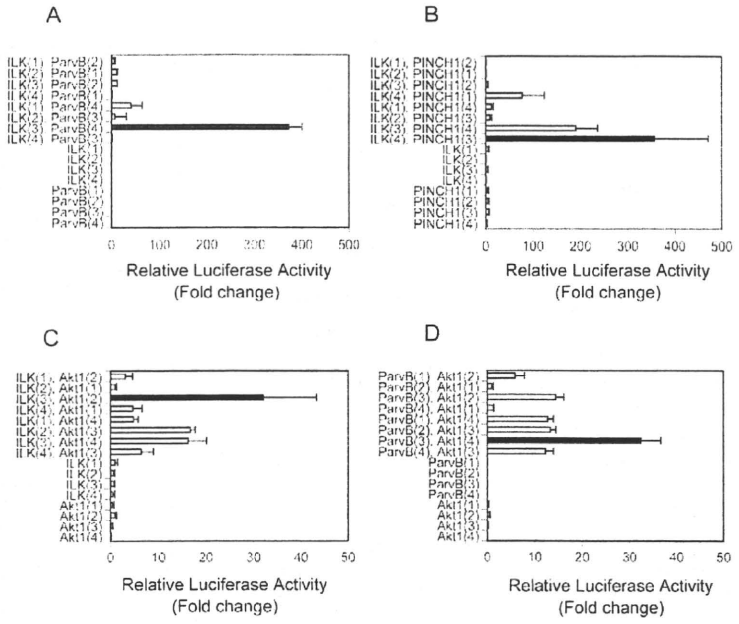

Fig. 2. Relative luciferase activity in eight luciferase complementation pairs. The optimized pair (black bar) found was for the following combinations: (**A**) ILK and ParvB, (**B**) ILK and PINCH1, (**C**) ILK and Akt1, (**D**) ParvB and Akt1. Numbers in parentheses represent the same four types of plasmids as in Fig. 1B.

of Akt1 with ParvB was much greater than that derived from the association of Akt1 with ILK, suggesting the preferential interaction of Akt1 with ParvB rather than ILK under living cell conditions. Maximum luminescent levels derived from the association of Akt1 with ParvB were in the range 800-1600 counts/pixels (50- to 100-fold higher than that observed for Akt1 and ILK). Kinetic analysis of Akt1-ILK complex formation showed an upward-bulging curve, with maximum luminescence levels being observed for 40-50 minutes following the addition of D-luciferin. Control expression using intact luciferase reached a peak immediately following the addition of D-luciferin (supplementary material Fig. S2). These results indicate that real-time complementary imaging can reveal

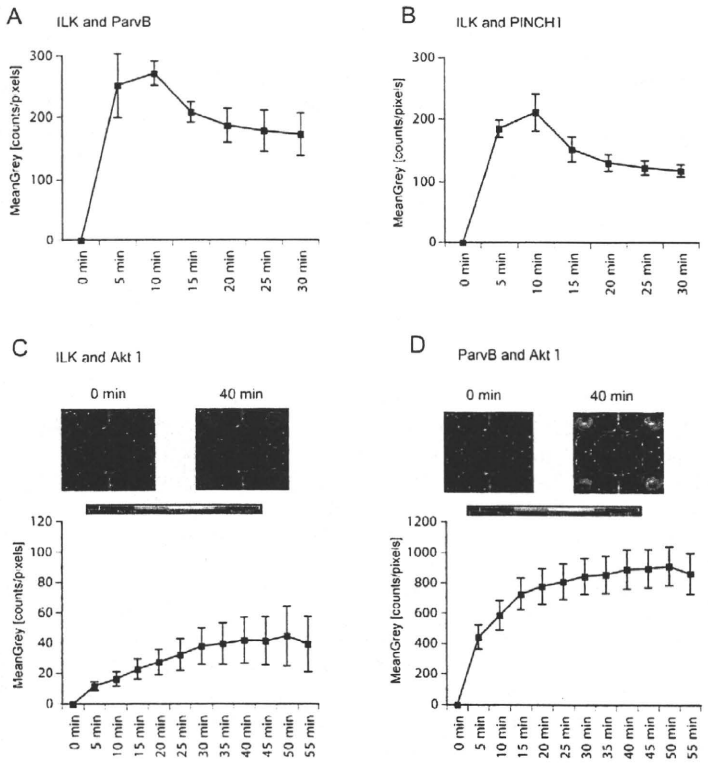

Fig. 3. Kinetic luminescence signals of the optimal luciferase complementation pair in 293T cells. (**A**) ILK and ParvB, (**B**) ILK and PINCH1, (**C**) ILK and Akt1, (**D**) ParvB and Akt1. The complementation imaging assay was performed under the same conditions pertaining to panels A and B, or C and D. With respect to Akt1-ILK and Akt1-ParvB complex formation, representative pseudo-color images (four-part) of a 24-well plate showed maximal luminescence signals 40 minutes following the addition of D-luciferin (upper panels). Notably, the combination of ParvB with Akt1 provided stronger signals than the combination of ILK with Akt1.

characteristics unique to each target protein-protein interaction, in this case suggesting that ParvB might be an important connecting molecule in the ILK-Akt/PKB signaling pathway.

Functional complementation imaging demonstrated ParvB-Akt1 interaction following serum stimulation

In an effort to glean insight into the role of ParvB, we set out to determine whether the ParvB-Akt1 interaction was modified following serum-triggered induction. As depicted in Fig. 4A, representative pseudo-color images based on the split luciferase system revealed that photon flux derived from the interaction of ParvB with Akt1 increased under serum-rich conditions and diminished under serum-starved conditions or in the presence of a PI3K inhibitor. Consistent with these findings were the results obtained when investigating the kinetics of the ParvB-Akt1 interaction under serum-starved conditions or in the presence of a PI3K inhibitor with serum at 1-minute intervals following the addition of D-luciferin (Fig. 4B-D). The kinetic curves were logarithmic in shape. Maximum photon flux for the ParvB-Akt1 interaction for each condition was observed 20-40 minutes following serum stimulation. Serum-rich treatment increased photon flux derived from the interaction of ParvB with Akt1 (Fig. 4B). PI3K inhibitors such as LY294002 and wortmannin suppressed serum-triggered induction (Fig. 4C,D). Employment of a dual-luciferase assay also demonstrated that luciferase activity arising from the ParvB-Akt1 interaction in lysate cells was similar to photon flux in live cells (Fig. 4E). However, with respect to the ILK-Akt1 interaction and a control plasmid encoding full-length firefly luciferase, there was no significant change in luciferase activity under serum-starved or PI3K inhibitor conditions with serum (supplementary material Fig. S3A,B). These results demonstrate that serum stimulation increases photon flux derived from the interaction of ParvB with Akt1, suggesting that PI3K inhibitors attenuate the serum-stimulated interaction between ParvB and Akt1.

Interaction between ILK and Akt1 is affected by ParvB mRNA levels

Because ILK-dependent phosphorylation is regulated by PI3K, it is possible that the inhibition of PI3K activity decreases ILK activity, which subsequently impairs the phosphorylation of putative ILK substrates (Delcommenne et al., 1998). One reliable marker that relates to ILK activity concerns the phosphorylation levels of Akt/PKB (Legate et al., 2006). Given the preferential association of ParvB with Akt1, we set out to determine whether ParvB levels regulate the interaction between ILK and Akt1. NIH3T3 cells were transfected with a reporter plasmid encoding the optimal split-luciferase complementation pair ILK-ParvB (Fig. 5A) and then subjected to siRNA-mediated ParvB knockdown. The knockdown efficiency of two types of mouse ParvB siRNAs (ParvB1 and ParvB2) is shown in Fig. 5B. These siRNAs were transfected into NIH3T3 cells stably overexpressing the complementation plasmid pair ILK-ParvB (see Fig. 5A) and the luminescence photon kinetics were evaluated (Fig. 5B). ParvB knockdown using siRNA decreased photon emission associated with ILK-ParvB association (siRNA ParvB2 was able to reduce approximately 50% of the photons derived from the interaction of ParvB with ILK). We then evaluated the extent of ILK-Akt1 complex formation with loss of ParvB using both luciferase complementation imaging and a co-immunoprecipitation assay. 293T cells were transfected with the optimal complementation plasmid pair ILK-Akt1 and then subjected to ParvB knockdown using siRNA ParvB2. As depicted in Fig. 5C,

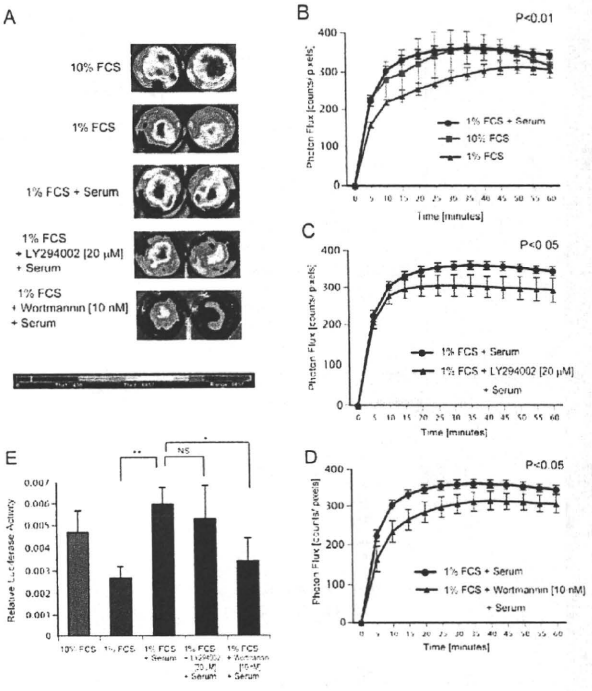

Fig. 4. Kinetics of luciferase complementation imaging for ParvB-Akt1 complex formation under different conditions. (**A**) Representative pseudo-color luminescence images emitted by the interaction between ParvB and Akt1 under either serum-starved conditions or in the presence of PI3K inhibitor (LY294002 or wortmannin) 20 minutes following serum stimulation. (**B**) Kinetic interaction between ParvB and Akt1 under serum-starved conditions following serum stimulation. 1% FCS versus 1% FCS plus serum. (**C**,**D**) Kinetic interaction between ParvB and Akt1 in the presence of PI3K inhibitors following serum stimulation: (C) 20 μM LY294002; (D) 10 nM wortmannin. 1% FCS plus serum versus 1% FCS plus serum plus PI3K inhibitor. (**E**) Relative luciferase activity for the interaction between ParvB and Akt1 20 minutes post-serum stimulation with or without PI3K inhibitors (LY294002 or wortmannin) All data are presented as a mean ± s.d. determined from the analysis of more than three independent experiments. NS, not statistically significant, $^{**}P<0.01$, $^{*}P<0.05$, ANOVA followed by post hoc tests or Student's *t*-test.

we investigated the kinetics of photons derived from the interaction of ParvB with Akt1 under ParvB knockdown conditions at 1-minute intervals following serum stimulation. Interestingly, siRNA ParvB led to an increase in photon flux associated with the ILK-Akt1 interaction. To provide further evidence showing that ParvB might regulate the ILK-Akt interaction, we performed a co-immunoprecipitation assay. 293T cells were transfected with the luciferase complementation plasmid pair ILK-ParvB (Fig. 5A) and then subjected to ParvB knockdown using siRNA ParvB2 (Fig. 5B). Overexpressed ILK and ParvB were precipitated with anti-phospho-Akt (Ser473) antibodies and precipitates were analyzed by western blotting using antibodies against ILK, ParvB, total-Akt and phospho-Akt (Ser473). As shown in Fig. 5D, decreased ParvB protein levels resulted in increased interaction between ILK and phospho-Akt (Ser473). These results suggest that ParvB might act as a potential modulator of the signal transduction associated with the ILK-Akt/PKB complex.

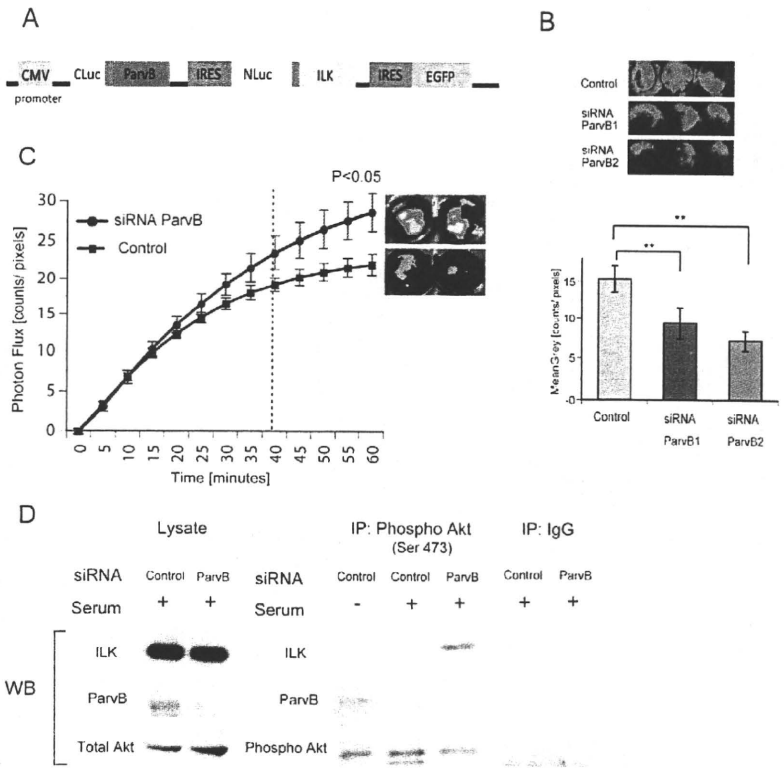

Fig. 5. Interaction between ILK and Akt1 under ParvB knockdown conditions. (**A**) Schematic representation of one expression vector encoding the optimal luciferase complementation pair ILK and ParvB. (**B**) ParvB knockdown by siRNA-inhibited luminescence signals in NIH3T3 cells overexpressing the optimal luciferase complementation pair ILK and ParvB. Representative pseudo-color images (triplicate) of a 24-well plate (the upper panel) and its quantification (the lower panel). (**C**) 293T cells were transfected with the optimal luciferase complementation plasmid pair ILK and Akt1, and then treated with ParvB siRNA. The graph represents photon-derived kinetics of the interaction between ILK and Akt1 following serum stimulation (left panel). Representative pseudo-color luminescence images (right panel) of a 12-well plate 40 minutes post-stimulation (broken line). (**D**) The plasmid encoding the optimal luciferase complementation pair ILK and ParvB (A) was transfected into 293T cells, and cells were then treated with ParvB siRNA. Cell lysates were precipitated (IP) using anti-phospho-Akt (Ser473) antibodies and control IgG antibody, and then subjected to western blotting (WB) using anti-ILK, anti-ParvB, anti-Akt and anti-phospho-Akt (Ser473) antibodies. All data are presented as a mean ± s.d. (**P<0.01, ANOVA followed by post hoc tests or Student's t-test).

ParvB knockdown increased HIF-1 and VEGF-A expression levels

We showed above that ParvB protein levels regulate the ILK-Akt1 interaction following serum stimulation. It has been demonstrated that HIF-1α is an important downstream effector that acts through the PI3K-Akt/PKB signaling pathway (Jiang et al., 2001). Furthermore, HIF-1α can regulate the expression of VEGF (Forsythe et al., 1996; Liu et al., 1995). In an effort to examine the effect of ParvB downregulation on downstream targets of the ILK-Akt signaling pathway, HIF-1α and VEGF protein expression levels were investigated following siRNA-mediated ParvB knockdown. ParvB is ubiquitously expressed, but enriched in heart and skeletal muscle (Bendig et al., 2006; Sepulveda and Wu, 2006). We transfected rat ParvB-specific siRNA into rat cardiomyocytes and confirmed the knockdown effect of ParvB (Fig. 6A). Western blot analysis demonstrated increased expression levels of endogenous HIF-1α and VEGF-A with ParvB knockdown in rat cardiomyocytes. HIF-1α and VEGF-A expression levels were quantified and statistically analyzed (Fig. 6B,C).

In an effort to further investigate the increase in HIF-1α expression induced by siRNA ParvB, another reporter plasmid was employed containing oxygen-dependent degradation (ODD)-luciferase, which comprises the ODD domain of HIF-1α fused to luciferase. Because the stability of HIF-1α is tightly regulated through the ODD domain (Harada et al., 2002), luciferase activity associated with the fusion protein reflects stabilized HIF-1α levels. ODD-luciferase cDNA was subcloned into the pcDNA3.1 expression plasmid (Fig. 6D) and transfected into NIH3T3 cells. ODD-luciferase-expressing stable transformants were obtained following G418 selection. We then introduced siRNA ParvB1 or ParvB2 into the ODD-luciferase-expressing NIH3T3 transformants. As shown in Fig. 6E, ParvB knockdown resulted in a marked increase in the expression of ODD-luciferase. Moreover, the hypoxia mimetics $CoCl_2$ and desferrioxamine (DFO) also increased ODD-luciferase-derived photon flux in the NIH3T3 transformants (Fig. 6F). To further confirm the requirement for ILK in the induction of HIF-1α stability under loss of ParvB, both siRNA ParvB1 and siRNA ILK were introduced into ODD-luciferase-expressing NIH3T3 transformants. As shown in Fig. 6G, knockdown using both ParvB and ILK did not increase ODD-luciferase-derived photon flux in the NIH3T3 transformants (Fig. 6G).

Taken together, these results indicate that decreased levels of ParvB stabilize HIF-1α in the presence of ILK, suggesting that ParvB downregulation might mimic hypoxic conditions through the ILK-Akt/PKB signaling pathway.

Discussion

Complementation strategies using an imaging probe with appropriate protein reconstitution enable visualization of steady-state complexes formed between protein pairs. One of the benefits associated with the use of these techniques is the exclusion of certain secondary effects or potential artifacts caused by cell lysis (Kerppola, 2006a; Kerppola, 2006b). Of the available complementation strategies, luciferase-based luminescence complementation imaging can be employed as a facile and broadly applicable approach (Luker et al., 2004). In this study, we demonstrated two complementary methods employing fluorescent or luminescent protein probes. Both imaging methods required that eight combinations of reporter plasmids be examined to determine optimal signal gain from the target protein-protein interaction.

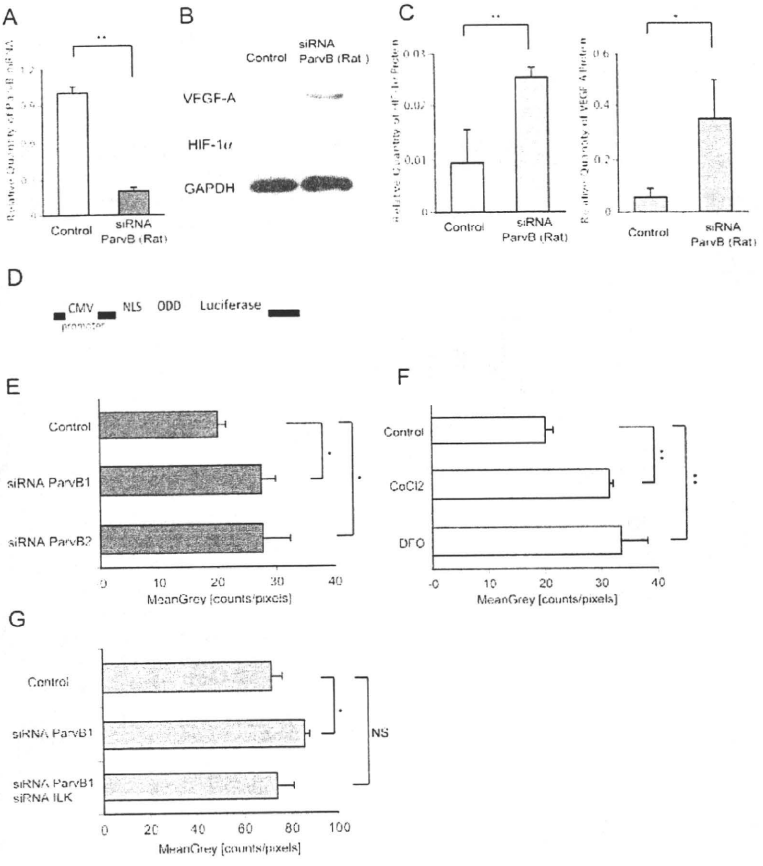

Fig. 6. Stabilization of HIF-1 and increased expression of VEGF-A under loss of ParvB. (**A**) Quantitative real-time RT-PCR for ParvB in rat cardiomyocytes following treatment with rat ParvB-specific siRNA. (**B**) siRNA-mediated ParvB knockdown increased protein expression levels of HIF-1α and VEGF-A in cardiomyocytes following serum stimulation. (**C**) Quantitative analysis (using ImageJ software) of endogenous HIF-1α (left panel) and VEGF-A (right panel) expression levels from the siRNA-mediated ParvB knockdown experiments shown in B. (**D**) Schematic representation of the reporter plasmid construct encoding a fusion protein, ODD-luciferase, which comprises part of the ODD domain of HIF-1α fused to luciferase (Harada et al., 2002). (**E**) siRNA-mediated ParvB knockdown increased photon count in NIH3T3 cells overexpressing ODD-luciferase. (**F**) Hypoxia mimetics $CoCl_2$ (100 μM) and DFO (20 μM) increased luminescent signals in NIH3T3 cells overexpressing ODD-luciferase. (**G**) Double-knockdown using ParvB- and ILK-specific siRNAs did not increase ODD-luciferase-derived photons in the NIH3T3 transformants. All data are presented as a mean ± s.d. determined from the analysis of more than three independent experiments (**P<0.01, *P<0.05, ANOVA followed by post hoc tests or Student's t-test).

Although fluorescence complementation enabled visual observation of the actual protein interactions, it might not necessarily allow comparison of protein-protein interactions in living cells under the microscope. By contrast, luminescence complementation enables comparison of even weak protein interactions under almost real-time conditions by quantifying luminescent signals with a high signal-to-noise ratio. Furthermore, employment of the luciferase complementation strategy allows the observation of rapid changes in target protein interactions in subcellular compartments under various conditions. In fact, our extensive complementary studies demonstrated that ParvB preferentially binds to Akt1 rather than ILK under living cell conditions. Moreover, luciferase complementation imaging revealed that real-time changes in photon-based kinetics associated with the ParvB-Akt1 interaction were consistent with results obtained following the use of extracellular stimuli, such as growth factors and associated signal inhibitors. Thus, employing the complementation strategy with appropriate probes could provide unique findings that reflect real-time cellular responses to external stimuli. Based on the current studies, employment of functional molecular imaging using complementary methods promises to be a beneficial strategy for the exploration of molecular mechanisms pertaining to signal transduction.

The ILK-associated protein complex is profoundly involved in altering the flux of the PI3K-Akt/PKB signaling pathway (see Fig. 7). ILK-dependent phosphorylation is regulated in a PI3K-dependent manner. PI3K inhibitors reduce ILK activity and impair the phosphorylation of putative ILK substrates in cell culture (Delcommenne et al., 1998). ParvB is a binding partner of ILK and the CH2 domain of ParvB is phosphorylated by ILK. These findings suggest that ParvB probably plays a role in actin cytoskeleton remodeling and cell spreading with its binding partners, α-actinin and αPIX (Mongroo et al., 2004; Yamaji et al., 2004; Yamaji et al., 2001). One new finding in our study showed that the real-time photon-based kinetics of the ParvB-Akt interaction correlated with results obtained following the use of extracellular stimuli, such as the presence of serum with or without PI3K inhibitors (Fig. 4). Moreover, decreased levels of ParvB protein were associated with a marked increase in photons derived from the ILK-Akt interaction (Fig. 5C,D). Although the interaction between ParvB and Akt had not been reported before this study, ParvB might cooperate with Akt and play a regulatory role in ILK-Akt complex formation (Fig. 7).

The role of ParvB in relation to Akt/PKB downstream effectors had not previously been sufficiently addressed. In this study, we demonstrated that siRNA-mediated ParvB knockdown increased HIF-1α and VEGF expression in rat cardiomyocytes (Fig. 6B,C). In particular, we showed that the phenomenon was correlated with HIF-1α stabilization. In our luciferase-based real-time imaging, ODD-luciferase expression levels increased with siRNA-mediated ParvB knockdown, firmly supporting the notion of HIF-1α stabilization (Fig. 6E). Furthermore, the hypoxia mimetics $CoCl_2$ (100 μM) and DFO (20 μM) increased luminescent signals in ODD-luciferase-overexpressing NIH3T3 cells. The effect of ParvB knockdown was the same as that of hypoxia mimetic agents. However, knockdown using both ParvB and ILK siRNAs did not increase luminescent

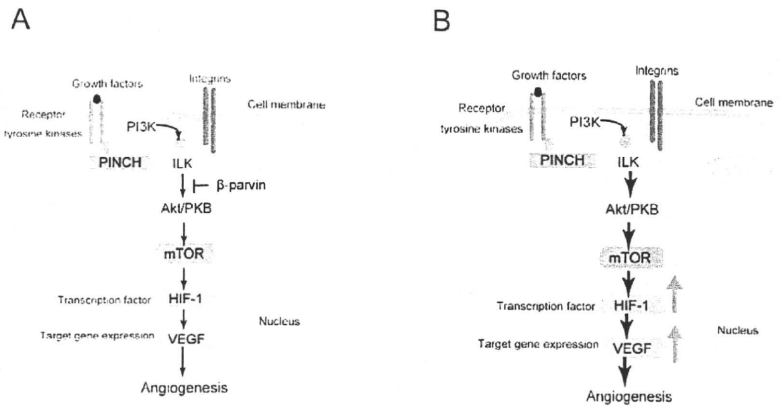

Fig. 7. Schematic representation of the role of ParvB in the ILK-Akt/PKB signaling pathway. (**A**) The normal and physiological state. ParvB might act as a modulator to prevent the transmission of excess signals. (**B**) The ParvB-depleted state. Without regulation of ParvB, excess signals might be transmitted in an uncontrolled manner to downstream targets.

signals in ODD-luciferase-overexpressing NIH3T3 cells (Fig. 6G). These results suggest that ParvB expression levels potentially control HIF-1α levels in the presence of ILK and that HIF-1α levels subsequently alter the expression of target genes such as VEGF-A. Taken together with the results presented here, one possible scenario can be outlined (Fig. 7): growth factors trigger ILK-Akt/PKB signaling activation and consequently ParvB could be phosphorylated by activated ILK, leading to increased interaction between ParvB and Akt. In the normal and physiological state, ParvB might act as a modulator to prevent the transmission of excess signals, such as those derived from growth factors, in the ILK-Akt/PKB signaling cascade (Fig. 7A). However, without regulation of ParvB, excess signals might be transmitted in an uncontrolled manner to downstream targets such as HIF1-α or VEGF (Fig. 7B). The notion of ParvB acting as a modulator might be supported by the finding that ParvB is downregulated in breast cancer (Mongroo et al., 2004).

With respect to the role of ParvB in ILK–Akt/PKB–HIF-1α signaling, it has been demonstrated that loss of ParvB expression upregulates ILK activity in tumors (Mongroo et al., 2004) and that ILK activation triggers a cascade of Akt/PKB phosphorylation events in tumor cells (Majumder et al., 2004). Because it has been reported that transcriptional responses to Akt/PKB activation are involved in the mTOR-dependent regulation of HIF-1α in an Akt-driven prostate intraepithelial tumor, ParvB might be involved in HIF-1α stabilization via ILK-Akt/PKB signaling in tumor cells. Thus, it is believed that our results are consistent with the role of ParvB in tumor cells.

Although further investigations might be necessary given these findings, employment of the complementary protein imaging strategy enabled the visualization and quantification of protein-protein interactions. This approach allowed the detection of real-time alterations in ILK-Akt signaling under conditions involving extracellular stimulation of living cells. These compelling data demonstrate that ParvB plays a regulatory role in ILK-Akt/PKB-HIFα signaling.

Materials and Methods

cDNAs and plasmid construction

For the isolation of ILK, ParvB, PINCH1 and Akt1 cDNA (GenBank accession numbers: NP_034692, NM_133167, NM_026148 and NM_009652, respectively), total RNA was extracted from the heart of BALB/c mice using ISOGEN (Nippon Gene, Tokyo, Japan) following the manufacturer's instructions. 1 μg of total RNA was reverse transcribed using random hexanucleotide primers and SuperScript III (Invitrogen Carlsbad, CA) according to the manufacturer's instructions. The entire coding sequence of these cDNAs was amplified by PCR using appropriate cloning primers (supplementary material Table S1). PCR was performed using EX Taq polymerase (Takara Bio, Otsu, Japan) as follows: 94°C for 2 minutes, 59°C for 1 minute, 72°C for 2 minutes, followed by 30 cycles of 94°C for 30 seconds, 62°C for 30 seconds and 72°C for 1 minute, with a final extension step at 72°C for 5 minutes. PCR products were cloned into 2.1 TOPO vector (Invitrogen, Carlsbad, CA). To detect KG fluorescent signals formed by the protein-protein interactions, ILK, ParvB, PINCH1 and Akt1 cDNAs were subcloned into phmKGN-MC, phmKGC-MC, phmKGN-MN and phmKGC-MN plasmids of the Fluo-chase kit (Medical & Biological Laboratories, Woburn, MA), which included the Kozak consensus sequence.

For the split firefly luciferase complementation assay, optimal pairs of N- and C-terminal cDNA fragments were amplified by PCR from pGL4.10 plasmid DNA (Promega, Madison, WI). The N- or C-terminal cDNA fragment was inserted into the pcDNA3.1 expression vector (Invitrogen). ILK, ParvB, PINCH1 and Akt1 cDNAs were fused in-frame to the N-terminal luciferase fragment (NLuc) or the C-terminal luciferase fragment (CLuc) containing a linker sequence.

Both ParvB cDNA fragments comprising N-terminal CLuc (CLuc-linker-ParvB) and ILK with N-terminal NLuc (NLuc-linker-ILK) were inserted into the pILES2-EGFP expression vector (Clontech Laboratories, Palo Alto, CA). An internal ribosomal entry site (IRES) sequence was inserted upstream of the start site of the NLuc-linker-ILK cDNA.

All PCR primer sequences for cDNA cloning and subcloning are shown in supplementary material Table S1.

Cell culture and transfection

NIH3T3 and 293T cells were maintained in Dulbecco's Modified Eagle's Medium (DMEM; Sigma Chemical Co., St Louis, MO) supplemented with 10% heat-inactivated fetal calf serum (FCS), 1 mM sodium pyruvate, 10 mM HEPES buffer, 2 mM glutamine, 100 units/ml penicillin G and 100 μg/ml streptomycin sulfate. Hearts from Wistar rat neonates were removed under a microscope, minced and digested four times at 37°C using a mixture of 1 mg/ml collagenase (Worthington Biochemical Co, Lakewood, NJ) and Hank's solution. Cardiac cells were neutralized and washed by low-speed centrifugation in 10% FCS-DMEM. After enzymatic digestion of their tissues, a cardiomyocyte fraction was prepared by Percoll gradient centrifugation (GE Healthcare). Cardiomyocytes were plated on wells pre-incubated with FCS.

Transient transfection was performed with an 80% confluent cell culture of 293T and NIH3T3 cells using Lipofectamine 2000 or Lipofectamine LTX (Invitrogen) according to the manufacturer's instructions. For serum stimulation, transfected cells were serum starved in 1% FCS for 18-20 hours and followed by FCS addition immediately before the assay. For PI3K inhibition, cells were pretreated with LY294002 (Sigma) or wortmannin (Sigma) at the concentration specified in the figure legends for 2 hours before the assay.

For the isolation of stable transformants that express the optimal complementation pair ILK and ParvB with EGFP (see Fig. 5A) and ODD-luciferase (Harada et al., 2002) (see Fig. 6D), NIH3T3 cells were grown in 10% FCS-DMEM containing 1000 μg/ml G418 at 2 days post-transfection. Following 21 days of G418 selection, neomycin-resistant colonies were isolated.

For the siRNA experiments, ParvB-specific siRNA duplexes, ILK-specific siRNA duplexes and an unrelated siRNA duplex as a control were purchased from Invitrogen. The siRNA transfection was performed using Lipofectamine 2000 (Invitrogen) according to the manufacturer's instructions. The final siRNA concentration was 20-40 nM.

Complementation imaging assay

The fluorescence complementation assay was performed using the Fluo-chase Kit (Medical & Biological Laboratories). 293T cells were co-transfected using the split-mKG vector system according to the manufacturer's instructions. Cells were inspected and photographed at 36-48 hours post-transfection using a fluorescent microscope equipped with a UV light source (excitation 470-495 nm; emission 510-550 nm).

For the luciferase-based complementation imaging, firefly luciferase cDNA was split into two fragments. 293T cells were co-transfected with the appropriate eight pairs of constructed plasmids (see Fig. 1C). Cells were plated and then transiently co-transfected with the appropriate pairs of plasmids using Lipofectamine 2000 (Invitrogen). At 36-40 hours after transfection, photon flux from the cells was measured using the NightOWL imager at 1-minute intervals following the addition of D-luciferin (potassium salt; Biosynth, Postfach, Switzerland). Cells were also assayed at 36-40 hours following transfection using the dual-luciferase reporter assay system (Promega) according to the manufacturer's instructions.

Immunoprecipitation and western blotting

293T cells were transfected with the constructed plasmid encoding the optimal luciferase complementation plasmid ILK-ParvB. Cells were lysed with a lysis buffer (1% Triton X in 50 mM HEPES, pH 7.4, containing 150 mM NaCl, 1 mM Na_3VO_4, 50 mM NaF and protease inhibitors). Cell lysates were incubated overnight at 4°C with anti-phospho-Akt (Ser473) antibodies (Cell Signaling Technology, Beverly, MA) and then mixed with protein-G agarose beads (GE Healthcare, Piscataway, NJ). Precipitates were washed four times and then subjected to western blotting.

For western blot analysis, cells were lysed 2-3 days following transfection with a lysis buffer (50 mM Tris-HCl, pH 7.4, 1% NP-40, 0.25% sodium deoxycholate, 0.1% SDS, 150 mM NaCl, 1 mM EDTA, 1 mM Na_3VO_4, 1 mM NaF and protease inhibitors). Cell lysates were subjected to 5-20% SDS-PAGE and then transferred onto polyvinylidene difluoride membranes. Blots were blocked using 2% bovine serum albumin (Sigma) or 5% ECL blocking agent (GE Healthcare) in TBST buffer (20 mM Tris-HCl, 150 mM NaCl and 0.1% Tween 20). Membranes were then incubated overnight at 4°C with target primary antibodies in the blocking buffer at a dilution recommended by the manufacturer [phospho-Akt (Ser473), Akt and ILK: Cell Signaling Technology, Beverly, MA; HIF-1α: Chemicon, Temecula, CA; VEGF-A: Immuno-Biological Laboratories Co, Gunma, Japan; luciferase: Promega; ParvB and GAPDH: Santa Cruz Biotechnology Inc, Santa Cruz, CA]. Membranes were washed extensively in TBST buffer and then incubated with Clean-Blot IP Detection Reagent HRP (Thermo Fisher Scientific Inc., Rockford, IL), anti-rabbit IgG (Cell Signaling Technology), anti-goat IgG (Santa Cruz Biotechnology) or protein A (Bio-Rad, Hercules, CA) for 1 hour in TBST buffer. Membranes were finally washed with TBST buffer and signals were visualized using ECL plus (GE Healthcare).

Expression and purification of recombinant proteins

The ParvB fragment generated by PCR was cloned between the *Bam*HI and *Eco*RI restriction sites of pGEX-6P-1 (GE Healthcare). GST-ParvB and GST were expressed in *Escherichia coli* BL21 (DE3) and purified using GST Bind Kits (Novagen, Darmstadt, Germany) according to the manufacturer's instructions.

GST pull-down assay

For the pull-down assay, 5 μg of either GST or GST-ParvB mixed with 1 μg His-tagged Akt1 (Invitrogen) were bound to glutathione-coated agarose beads in 500 μl of binding buffer (150 mM NaCl, 50 mM HEPES, 0.1% NP-40, pH 7.4, 1 mM dithiotreitol) for 2 hours at 4°C. Bound proteins were washed three times and eluted with SDS sample buffer, separated by SDS-PAGE, and detected by western blotting and Coomassie brilliant blue (CBB) staining.

Quantitative real-time RT-PCR

Total RNA was isolated using ISOGEN (Nippon Gene Co.) according to the manufacturer's instructions. 1 μg of total RNA was reverse transcribed with oligo-dT primers using SuperScript III (Invitrogen) according to the manufacturer's instructions. ParvB gene expression was quantified using iQ SYBR Green Supermix (Bio-Rad). Each assay was performed in triplicate. ParvB transcript levels were determined as expression levels relative to 18S rRNA. The following primers were used: rat ParvB, 5′-TTGTCCCCCTTCACAACTTC-3′ and 5′-GTGTAAAG-GACCCGCAGAGT-3′; 18S rRNA, 5′-GTAACCCGTTGAACCCCATT-3′ and 5′-CCATCCAATCGGTAGTAGCG-3′. Each experiment was performed three times with similar results.

Statistics

Comparisons between multiple groups were performed using ANOVA followed by post hoc tests or Student's *t*-test. A P value less than 0.05 was considered significant.

We thank J. Hotta, Y. Ohide and M. Kumagai for excellent technical assistance. This study was supported in part by a grant to T.M. from the Health and Labour Science Research Grants (Research on Biological Resources), a Grant-in-Aid for Scientific Research from the Japan Society for the Promotion of Science (JSPS; project number 20591326; 2008), and a grant from the Strategic Research Platform for Private Universities: matching fund subsidy from MEXT (2008-), and a Research Award to JMU Graduate Student (M.K.).

Supplementary material available online at
http://jcs.biologists.org/cgi/content/full/123/5/747/DC1

References

Alessi, D. R., James, S. R., Downes, C. P., Holmes, A. B., Gaffney, P. R., Reese, C. B. and Cohen, P. (1997). Characterization of a 3-phosphoinositide-dependent protein kinase which phosphorylates and activates protein kinase Balpha. *Curr. Biol.* **7**, 261-269.

Attwell, S., Mills, J., Troussard, A., Wu, C. and Dedhar, S. (2003). Integration of cell attachment, cytoskeletal localization, and signaling by integrin-linked kinase (ILK), CH-ILKBP, and the tumor suppressor PTEN. *Mol. Biol. Cell* **14**, 4813-4825.

Bachelder, R. E., Wendt, M. A., Fujita, N., Tsuruo, T. and Mercurio, A. M. (2001). The cleavage of Akt/protein kinase B by death receptor signaling is an important event in detachment-induced apoptosis. *J. Biol. Chem.* **276**, 34702-34707.

Bendig, G., Grimmler, M., Huttner, I. G., Wessels, G., Dahme, T., Just, S., Trano, N., Katus, H. A., Fishman, M. C. and Rottbauer, W. (2006). Integrin-linked kinase, a novel component of the cardiac mechanical stretch sensor, controls contractility in the zebrafish heart. *Genes Dev.* **20**, 2361-2372.

Delcommenne, M., Tan, C., Gray, V., Rue, L., Woodgett, J. and Dedhar, S. (1998). Phosphoinositide-3-OH kinase-dependent regulation of glycogen synthase kinase 3 and protein kinase B/AKT by the integrin-linked kinase. *Proc. Natl. Acad. Sci. USA* **95**, 11211-11216.

Feng, J., Park, J., Cron, P., Hess, D. and Hemmings, B. A. (2004). Identification of a PKB/Akt hydrophobic motif Ser-473 kinase as DNA-dependent protein kinase. *J. Biol. Chem.* **279**, 41189-41196.

Förster, T. (1959). 10th Spiers Memorial Lecture. Transfer mechanisms of electronic excitation. *Discuss. Faraday Soc.* **27**, 7-17.

Forsythe, J. A., Jiang, B. H., Iyer, N. V., Agani, F., Leung, S. W., Koos, R. D. and Semenza, G. L. (1996). Activation of vascular endothelial growth factor gene transcription by hypoxia-inducible factor 1. *Mol. Cell. Biol.* **16**, 4604-4613.

Harada, H., Hiraoka, M. and Kizaka-Kondoh, S. (2002). Antitumor effect of TAT-oxygen-dependent degradation-caspase-3 fusion protein specifically stabilized and activated in hypoxic tumor cells. *Cancer Res.* **62**, 2013-2018.

Hu, C. D., Chinenov, Y. and Kerppola, T. K. (2002). Visualization of interactions among bZIP and Rel family proteins in living cells using bimolecular fluorescence complementation. *Mol. Cell* **9**, 789-798.

Jiang, B. H., Jiang, G., Zheng, J. Z., Lu, Z., Hunter, T. and Vogt, P. K. (2001). Phosphatidylinositol 3-kinase signaling controls levels of hypoxia-inducible factor 1. *Cell Growth Differ.* **12**, 363-369.

Kerppola, T. K. (2006a). Complementary methods for studies of protein interactions in living cells. *Nat. Methods* **3**, 969-971.

Kerppola, T. K. (2006b). Design and implementation of bimolecular fluorescence complementation (BiFC) assays for the visualization of protein interactions in living cells. *Nat. Protoc.* **1**, 1278-1286.

Legate, K. R., Montanez, E., Kudlacek, O. and Fassler, R. (2006). ILK, PINCH and parvin: the tIPP of integrin signalling. *Nat. Rev. Mol. Cell. Biol.* **7**, 20-31.

Liu, Y., Cox, S. R., Morita, T. and Kourembanas, S. (1995). Hypoxia regulates vascular endothelial growth factor gene expression in endothelial cells. Identification of a 5′ enhancer. *Circ. Res.* **77**, 638-643.

Luker, K. E., Smith, M. C., Luker, G. D., Gammon, S. T., Piwnica-Worms, H. and Piwnica-Worms, D. (2004). Kinetics of regulated protein-protein interactions revealed with firefly luciferase complementation imaging in cells and living animals. *Proc. Natl. Acad. Sci. USA* **101**, 12288-12293.

Majumder, P. K., Febbo, P. G., Bikoff, R., Berger, R., Xue, Q., McMahon, L. M., Manola, J., Brugarolas, J., McDonnell, T. J., Golub, T. R. et al. (2004). mTOR inhibition reverses Akt-dependent prostate intraepithelial neoplasia through regulation of apoptotic and HIF-1-dependent pathways. *Nat. Med.* **10**, 594-601.

Mongroo, P. S., Johnstone, C. N., Naruszewicz, I., Leung-Hagesteijn, C., Sung, R. K., Carnio, L., Rustgi, A. K. and Hannigan, G. E. (2004). Beta-parvin inhibits integrin-linked kinase signaling and is downregulated in breast cancer. *Oncogene* **23**, 8959-8970.

Paulmurugan, R., Umezawa, Y. and Gambhir, S. S. (2002). Noninvasive imaging of protein-protein interactions in living subjects by using reporter protein complementation and reconstitution strategies. *Proc. Natl. Acad. Sci. USA* **99**, 15608-15613.

Persad, S., Attwell, S., Gray, V., Mawji, N., Deng, J. T., Leung, D., Yan, J., Sanghera, J., Walsh, M. P. and Dedhar, S. (2001). Regulation of protein kinase B/Akt-serine 473 phosphorylation by integrin-linked kinase: critical roles for kinase activity and amino acids arginine 211 and serine 343. *J. Biol. Chem.* **276**, 27462-27469.

Rokudai, S., Fujita, N., Hashimoto, Y. and Tsuruo, T. (2000). Cleavage and inactivation of antiapoptotic Akt/PKB by caspases during apoptosis. *J. Cell Physiol.* **182**, 290-296.

Sepulveda, J. L. and Wu, C. (2006). The parvins. *Cell Mol. Life Sci.* **63**, 25-35.

Tan, C., Cruet-Hennequart, S., Troussard, A., Fazli, L., Costello, P., Sutton, K., Wheeler, J., Gleave, M., Sanghera, J. and Dedhar, S. (2004). Regulation of tumor angiogenesis by integrin-linked kinase (ILK). *Cancer Cell* **5**, 79-90.

Troussard, A. A., Mawji, N. M., Ong, C., Mui, A., St -Arnaud, R. and Dedhar, S. (2003). Conditional knock-out of integrin-linked kinase demonstrates an essential role in protein kinase B/Akt activation. *J. Biol. Chem.* **278**, 22374-22378.

Williams, M. R., Arthur, J. S., Balendran, A., van der Kaay, J., Poli, V., Cohen, P. and Alessi, D. R. (2000). The role of 3-phosphoinositide-dependent protein kinase 1 in activating AGC kinases defined in embryonic stem cells. *Curr. Biol.* **10**, 439-448.

Yamaji, S., Suzuki, A., Sugiyama, Y., Koide, Y., Yoshida, M., Kanamori, H., Mohri, H., Ohno, S. and Ishigatsubo, Y. (2001). A novel integrin-linked kinase-binding protein, affixin, is involved in the early stage of cell-substrate interaction. *J. Cell Biol.* **153**, 1251-1264.

Yamaji, S., Suzuki, A., Kanamori, H., Mishima, W., Yoshimi, R., Takasaki, H., Takabayashi, M., Fujimaki, K., Fujisawa, S., Ohno, S. et al. (2004). Affixin interacts with alpha-actinin and mediates integrin signaling for reorganization of F-actin induced by initial cell-substrate interaction. *J. Cell Biol.* **165**, 539-551.

European Cells and Materials Vol. 19 2010 (pages 13-21) ISSN 1473-2262

PRIMARY IMMUNE SYSTEM RESPONDERS TO *NUCLEUS PULPOSUS* CELLS: EVIDENCE FOR IMMUNE RESPONSE IN DISC HERNIATION

Kunihiko Murai[1]*, Daisuke Sakai[2,3], Yoshihiko Nakamura[3], Tomoko Nakai[3], Takashi Igarashi[1], Norimasa Seo[1], Takashi Murakami[4], Eiji Kobayashi[4], and Joji Mochida[2,3]

[1]Department of Anesthesiology and Intensive Care Medicine, Jichi Medical University, 3311-1 Yakushiji, Shimotsuke, Tochigi, 329-0498, Japan
[2]Department of Orthopaedic Surgery, Surgical Science, Tokai University School of Medicine, 143 Shimokasuya, Isehara, Kanagawa 259-1193, Japan
[3]Research Center for Regenerative Medicine, Tokai University School of Medicine, 143 Shimokasuya, Isehara, Kanagawa 259-1193, Japan
[4]Division of Organ Replacement Research, Center for Molecular Medicine, Jichi Medical University, 3311-1 Yakushiji, Shimotsuke, Tochigi, Japan

Abstract

Although intervertebral disc herniation and associated sciatica is a common disease, its molecular pathogenesis is not well understood. Immune responses are thought to be involved. This study provides direct evidence that even non-degenerated *nucleus pulposus* (NP) cells elicit immune responses. An *in vitro* colony forming inhibition assay demonstrated the suppressive effects of autologous spleen cells on NP cells and an *in vitro* cytotoxicity assay showed the positive cytotoxic effects of natural killer (NK) cells and macrophages on NP cells. Non-degenerated rat NP tissues transplanted into wild type rats and immune-deficient mice demonstrated a significantly higher NP cell survival rate in immune-deficient mice. Immuno-histochemical staining showed the presence of macrophages and NK cells in the transplanted NP tissues. These results suggest that even non-degenerated autologous NP cells are recognized by macrophages and NK cells, which may have an immunological function in the early phase of disc herniation. These findings contribute to understanding resorption and the inflammatory reaction to disc herniation.

Keywords: *Nucleus pulposus*, immune response, macrophage, natural killer cell, intervertebral disc, autoimmunity.

*Address for correspondence:
Kunihiko Murai
Department of Anesthesiology and Intensive Care Medicine,
Jichi Medical University,
3311-1 Yakushiji, Shimotsuke, Tochigi, 329-0498, Japan
Telephone Number: +81 285 58 7383
FAX Number: +81 285 44 4108
E-mail: murai.mane@jichi.ac.jp

Introduction

Resorption of herniated *nucleus pulposus* (NP) is a clinically demonstrated phenomenon during intervertebral disc herniation. In understanding the undefined pathogenesis of intervertbral disc herniation and sciatica, clarifying the molecular events that occur in resorption of NP is important. Nachemson (1969) reported decreased pH levels within and around a herniated lumbar disc and speculated that sciatica was caused by an inflammatory reaction surrounding the nerve root. Subsequently, various inflammatory chemical factors secreted from herniated NP, including tumor necrosis factor (TNF)-α (Weiler *et al.*, 2005; Le Maitre *et al., 2007*), interleukin (IL)-1β (Le Maitre *et al., 2007*) and nitric oxide (NO) (Katsuno *et al.*, 2008), have been implicated as causes of sciatica (McCarron *et al*, 1987; Geiss *et al.*, 2007). Further, the production of matrix metalloproteinases (MMPs) has been implicated in the resorption of the herniated NP (Doita *et al.*, 2001).

Bobechko and Hirsh (1965) and Gertzbein *et al.* (1975) reported that herniated NP tissue is recognized as a foreign antigen that induces an autoimmune response producing inflammation. Later, immunohistochemical (IHC) analyses of human herniated discs revealed the presence of infiltrated T cells (Park *et al.*, 2001), macrophages (Park *et al.*, 2001; Virri *et al.*, 2001), and antigen-antibody complexes in the NP (Satoh *et al.*, 1999). An *in vitro* co-culture model of macrophages and NP cells also showed the infiltration of macrophages and a decreased wet weight of the NP (Haro *et al.*, 2000). The expression of IL-6, -8, -12, and interferon (IFN)-γ suggests Th1 lymphocyte activation (Kang *et al.*, 1996; Burke *et al.*, 2002; Park *et al.*, 2002). Geiss *et al.* placed autologous porcine NP in subcutaneous titanium chambers and observed the infiltration of activated T and B cells (Geiss *et al.*, 2007), including IL-4-producing Th2 cells and γδ T cells (Geiss *et al.*, 2008). These results indicate both innate and acquired immune responses to the NP. Other studies (Park *et al.*, 2001; Jones *et al.*, 2008), however, have reported that NP cells undergo apoptosis and are phagocytised by macrophages without an immune response. Ikeda *et al.* (1996) investigated infiltrated cells consisting of macrophages and a small number of T cells, and proposed that extruded or sequestrated disc material

has the potential to be absorbed by phagocytes. It remains unclear from these reports whether immune responses are truly involved in disc herniation, and if so, which immune cells initiate the immune response.

In order to investigate whether an immune response is involved in disc herniation, fundamental research on NP cells and the immune system is required. The purpose of this study is to clarify the immune response to autologous NP cells and to identify the specific immune cells that initiate an immune response by using *in vivo* and *in vitro* rat models to assess the survival of NP cells exposed to immune system cells.

Materials and Methods

In vitro studies

Preparation of rat-tail NP cells. Male Sprague-Dawley (SD) rats (Nihon Charles River Co., Kanagawa, Japan) aged 10-12 weeks, were used for the colony forming inhibition assay (CFI), and male Lewis rats (Nihon Charles River) aged 10-12 weeks were used for the cytotoxicity assay. Following sacrifice, NP tissues were dissected from the whole tail and digested in 0.05% trypsin-ethylene diamine tetraacetic acid (EDTA; Gibco, Grand Island, NY, USA) for 15 minutes. The digestate was washed, passed through a 100 μm mesh cell strainer, the NP cells were collected by mild centrifugation (500Gx4min). These experiments were approved by the Animal Research Committee of Tokai University (071095) and conducted according to the guidelines for animal experiments.

Preparation of spleen cells. Autologous spleen cells were used as effector cells for the CFI assay and isogenous spleen cells were used for the cytotoxicity assay. Briefly, the spleens were removed, mashed and passed through a 100 μm mesh cell strainer. Red blood cells were haemolysed using 0.8% NH_3CL. The spleen cells were collected by mild centrifugation (500Gx4min). The spleen cells (10^7cells/ml) were then incubated in RPMI-1640 medium (Invitrogen, Grand Island, NY, USA) with 15% foetal bovine serum (FBS, Qualified FBS, Invitrogen) at 37°C for five hours with IL-2 (60 IU/ml; Imunase, Shionogi, Osaka, Japan).

Purification of T cells, natural killer (NK) cells and macrophages. For cytotoxicity assays, more than 10^8 of the spleen cells isolated from a Lewis rat were suspended in fluorescence-activated cell sorting (FACS) buffer (Facs Flow, Becton Dickinson (BD) Pharmingen, Tokyo, Japan) and incubated for 30 minutes at 4°C with saturating amounts of the following antibodies: CD3 (#550353, PE mouse anti-rat CD3, BD), CD4 (#550057 Pharmingen, APC mouse anti-rat CD4, BD), CD8 (#558824, Per CP mouse anti-rat CD8a, BD), CD161 (#550978, biotin mouse anti-rat CD161, BD). The labelled spleen cells were then separated into NK cells (CD161+), CD4+T cells (CD3+CD4+), CD8+T cells (CD3+CD8+), and macrophages (remaining CD3-) using a FACS Vantage (BD).

CFI assay. For the CFI assay, the suppressive effect of immune cells (effector cells) on colony formation by autologous NP cells (target cells) was assessed by a previously described method (Spitzer *et al.*, 1980). The NP cells isolated from SD rats (N=4) were immediately utilized for the assay procedures. NP cells ($6x10^3$) and autologous spleen cells were seeded for each E:T ratio of 0:1, 25:1, 50:1 and 100:1 in 6ml of 0.9% methylcellulose formation (MethoCult H4230 Stemcell Technologies, Vancouver, Canada) in a single tube, mixed completely, then we dispensed it by 1ml in 35mm dishes (n=4 for each E:T ratio). The dishes were incubated at 37°C in 5% CO2 and full humidity for 14 days without medium replacement, after which the number of NP colonies was scored at least twice for each dish using a tally board on the bottom of the dishes.

Cytotoxicity assay. For the cytotoxicity assay, NP cells from Lewis rats (N=2) were monolayer cultured in RPMI-1640 medium with 15% FBS for 10 days. The cells were labeled using calcein-AM (Dojin Chemical Institute, Kumamoto, Japan) for 60 minutes at 37°C without serum, washed, and seeded into 96-well V-bottomed plates (#4914, Matrix Technologies, Hudson, NH, USA) at $1x10^4$ cells/ well. Suspensions of purified isogenous NK cells, CD4+ T cells, CD8+ T cells, or macrophage cells were then added to wells at E:T cell ratios of 0:1, 25:1, 50:1 and 100:1 in a final volume of 200 μL/well in RPMI-1640 medium without serum (n = 4 for each ratio). The plate was centrifuged, then incubated in humidified air for eight hours at 37°C. After incubation, the plates were centrifuged and 100 mL of supernatant from each well was moved to another 96 well flat-bottomed plate in the same pattern, and was measured using a fluorescent plate reader (λ_{ex}=485 nm, λ_{em}=520 nm, Beckman Coulter, Brea, CA, USA). Cytotoxic activity was determined according to a modification of the ^{3}H-uridine labelling method described by Wang *et al.* (1993). Cytotoxicity was calculated as:

$$\%\,\text{cytotoxicity} = \frac{\text{experimental release} - \text{spontaneous release}}{\text{total release} - \text{spontaneous release}} \cdot 100 \quad (1)$$

Total release was obtained by detergent solubilisation in the presence of 1% Triton X-100 (GE Healthcare Japan, Tokyo, Japan). Spontaneous release means the fluorescence release of the pure NP cell groups. Fibroblastic cells from the *anulus fibrosus* was also analyzed as negative control.

In vivo study

For *in vivo* studies, intact rat NP tissues were transplanted with PBS into immunodeficient mice and wild type rats. The survival rate of the NP cells in the transplanted tissue was measured using the bioluminescence imaging (BLI) method described below to estimate the influence of immunity on NP cell survival. IHC staining was done on the NP tissues from the rat model to detect attracted immune cells, which would indicate the initiation of an immune response.

Transplantation of NP for the BLI study

For the BLI analysis, four male Lewis rats 10-12 weeks of

age were used as recipients of NP tissues for the Lewis to Lewis (Lew-Lew) group and four male 10-12-week-old NOD/Shi-*scid* mice (Nihon Charles River) served as recipients of NP tissues for the Lewis to NOD (Lew-NOD) group. Transgenic (Tg) male Lewis rats (8-10 weeks of age) whose tissues express luciferase produced by repeated crossing of Tg rats and confirmed in the *Organ Replacement Research Department in Jichi Medical University* were used as NP tissue donors. 100 μg of NP tissues were injected with 100 μL of PBS under the abdominal skin of recipients under general anaesthesia using 2-3% isoflurane. One donor was used for each recipient. The BLI study was conducted using a IVIS system (Xenogen Corp., Hopkinton, MA, USA) with LivingImaging acquisition and analysis software. Briefly, animals were anesthetized with isoflurane and given 125 mg/kg D-luciferin substrate (Biosynth AG, Staad, Switzerland). The animals were then placed in a light-tight chamber for imaging with a CCD camera. The photon counts from the peak luciferase activity were recorded. Luciferase activity was measured as photons emitted/second. Imaging studies were performed immediately after transplantation and at day 7, day 14 and day 21.

IHC staining

For IHC staining, male Lewis rats (n=6) were newly used as recipients of NP tissues. The transplantation procedure was the same as for the Lew-Lew group described above and one donor was used for each recipient (n=6). Two recipients were sacrificed at 5, 10, and 40 days after transplantation. In addition, two NOD mouse in BLI study was sacrificed at 26 days after transplantation. After fixation with 10% formalin for three days, a paraffin block was made though an alcohol-xylene-paraffin graded series. Five-micron thick paraffin sections were cut sagittally from the epidermis to the peritoneal membrane across the transplantation site, deparaffinized 5-μm sections first were rehydrated through xylene and graded alcohol series. For double-staining immunofluorescence, tissue slides were incubated overnight at 4°C with a primary monoclonal antibody to keratan sulphate (KS) (#270427-1, mouse anti-KS, Associates of Cape Cod, Falmouth, MA, USA), diluted 1:100 in PBS with 1% BSA, followed by incubation in darkness at room temperature for three hours with Alexa Fluor 488-conjugated anti-mouse IgG diluted 1:200. After washing with PBS, the slides were incubated overnight at 4°C in darkness with diluted (1:100) primary antibodies for rat T cells (#550353, PE mouse anti-rat CD3, BD), macrophages (#sc-9139, rabbit anti-rat CD68, Santa Cruz Biotechnology, CA, USA), or NK cells (#550978, Biotin mouse anti-rat CD161, BD). After washing with PBS, the slides with CD68 were incubated for 60 minutes in room temperature with anti-rabbit goat Alexa 594 antibody (Invitrogen); slides with CD161 staining were incubated for one hour with streptavidin-Alexa 594 (Invitrogen). All slides were then covered with Vectashield mounting medium with DAPI (H-1500, Vector Laboratories, Burlingame, CA, USA). Sample sections of day 5, day 10 and day 40 were also stained with HE and Safranin-O.

Data Analysis

All data are given as the mean ± standard deviation (SD). The statistics were processed by Excel Stat 2006 (SSRI, Tokyo, Japan). Two-factor analysis of variance (ANOVA) was employed to analyze the *in vitro and in vivo results*. The Mann-Whitney U-test was used to compare the results of the two groups in CFI assay. When significant differences were revealed by the ANOVA, *post hoc* comparisons were done. Statistical significance was defined as $p < 0.05$.

Results

***In vitro* study**

CFI assay. Spleen cells from SD rats were used as effector cells for autologous tail NP target cells. Colony formation assays showed two types of colonies that were identified as CFU-A (adherent) and CFU-NA (non-adherent) when counting colonies. Without effector cells (E:T cell ratio of 0:1), NP cells ($1x10^3$) formed CFU-NA colonies ranging in numbers from 82-118 (94.8±18.1) and CFU-A colonies ranging from 39-60 (48.3±9.6). When effector cells were added, NP cells ($1x10^3$) with an E:T cell ratio of 25:1 yielded CFU-NA colonies ranging from 26-31 (29.0±2.2) and CFU-A colonies ranging from 22-38 (28.3±6.8), an E:T cell ratio of 50:1 resulted in CFU-NA colonies ranging from 19-26 (22.8±3.0) and CFU-A colonies ranging from 19-34 (26.8±6.6) and an E:T cell ratio of 100:1 produced CFU-NA colonies ranging from 19-25 (21.0±2.8) and CFU-A colonies ranging from 18-27 (21.0±4.2). The suppressive effect of spleen cells was apparent (Fig. 1A). CFU-NA colonies were affected stronger than CFU-A colonies (Table 1). Microscopic examinations of CFU-NA

Table 1 Percentage of the number of colonies to the control (E:T cell ratio = 0:1)

E:T cell ratio	0:1	25:1	50:1	100:1
CFU-NA (%)	100	30.6±2.3	24.0±3.2	22.2±3.0
CFU-A (%)	100	58.5±14.2	55.4±13.7	43.5±8.8
p-value		p=0.021	p=0.021	p=0.019

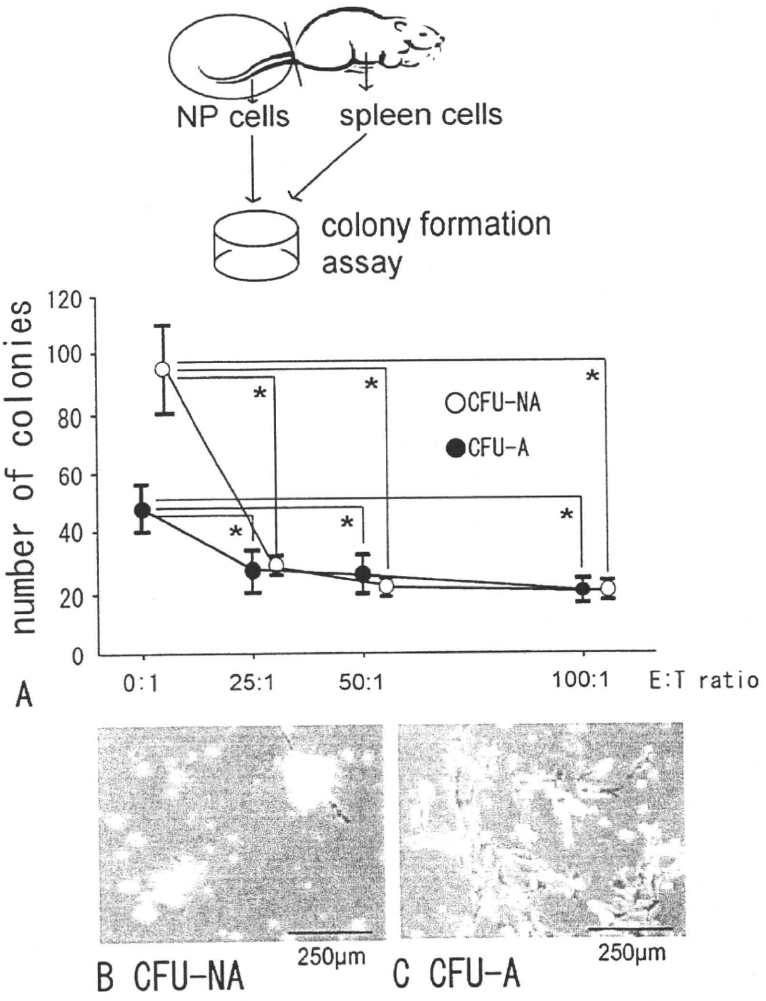

Fig. 1. (A) Results of CFI assay *in vitro*. Numbers of CFU-NA (open circle) and CFU-A (closed circle) colonies in the E: T ratio of 0:1, 25:1, 50:1 and 100:1 were counted at day 14. Colony formation of NP cells was suppressed by the addition of autologous spleen cells in both groups ($*p < 0.05$ compared with that in the E:T ratio of 0:1). (B) Attraction of spleen cells to CFU-NA. (C) Attraction of spleen cells to CFU-A. The larger number of spleen cells attracted to CFU-NA than that to CFU-A supports the result in our current study that CFU-NA is more sensitive to autologous spleen cells.

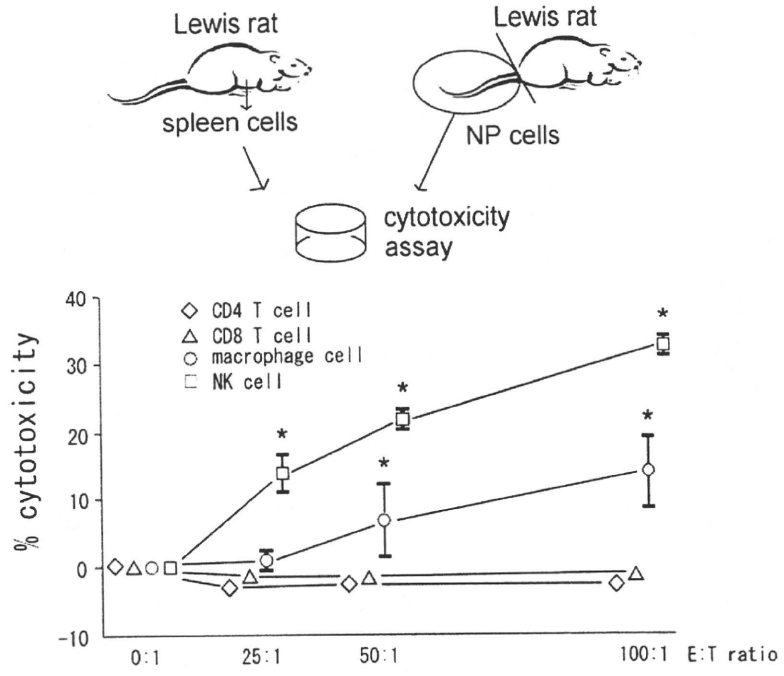

Fig. 2. Results of cytotoxicity assay *in vitro*. Cytotoxicity was calculated as follows,
Insert EQ1
0%=no cytotoxicity, 100%=maximum cytotoxicity as strong as detergent agent.
Cytotoxicity caused by NK cells and macrophages was suggested as a result of 8 hrs coculture ($*p < 0.05$ compared with that in the E:T ratio of 0:1).

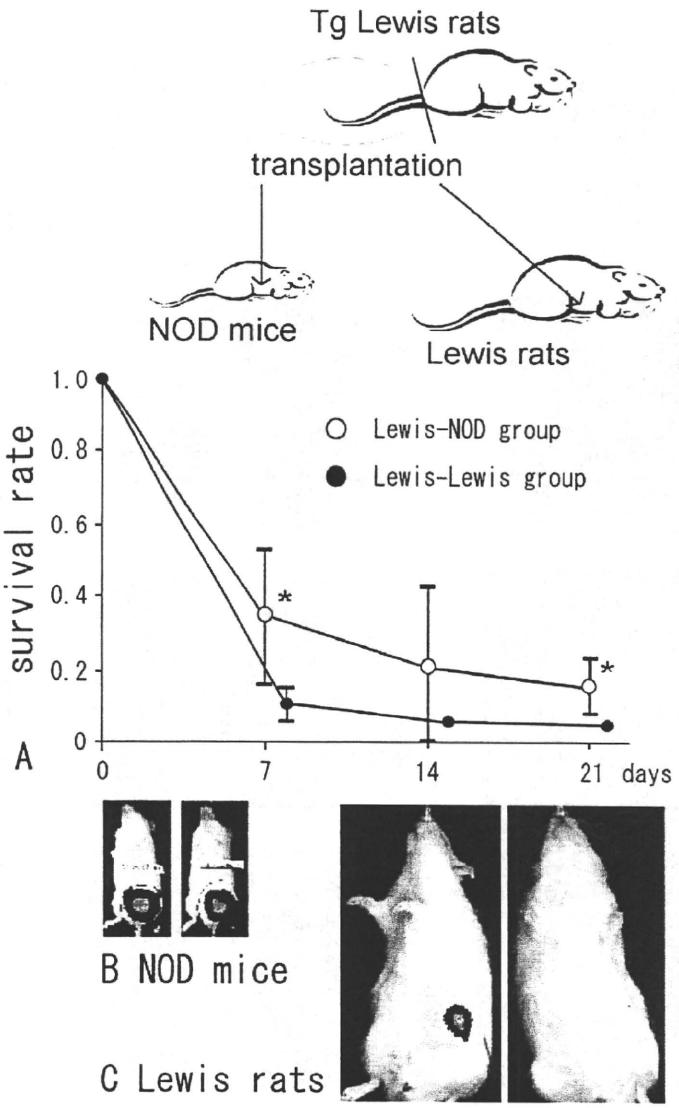

Fig. 3. (A) Survival rate of transplanted NP cells in Lewis rats and NOD mice (n=4, each). Closed circle indicates Lewis-Lewis group and open circle indicates Lewis-NOD group. Because intensity of luminescence is positively linear to the number of NP cells (data not shown), survival rate of NP cells was calculated as follows:

$$\text{Survival rate} = \frac{\text{Intensity of luminance after 7, 14 or 21 days}}{\text{Intensity of luminance just after transplantation}} \quad (2)$$

so that baseline value of survival rate (day 0) is "1". The survival rate was higher in the Lewis-NOD group than in the Lewis-Lewis group ($*p < 0.05$). (B) BLI imaging of NOD mouse at day 0 (left) and at day 90 (right). (C) BLI imaging of Lewis rat at day 0 (left) and at day 21 (right). NP cells hardly survived at day 21.

(Fig. 1B) and CFU-A (Fig. 1C) colonies revealed that larger numbers of spleen cells were attracted to CFU-NA colonies than to CFU-A colonies, further indicating that CFU-NA colony formation was more sensitive to the presence of spleen cells.

Cytotoxicity assay. From 10^8 Lewis rat spleen cells, $3.0x10^7$ CD4+T cells, $2.0x10^7$ CD8+T cells, $1.0x10^7$ macrophages and $6.0x10^6$ NK cells were sorted by FACS with data showing that more than 95% of the cells were alive.

Cytotoxicity to autologous NP cells was proportional to the E:T cell ratio in NK cells and macrophages (Fig. 2). At an E:T cell ratio of 100:1, cytotoxicity was 31-35% in NK cells and 9-20% in macrophages. Significant cytotoxicity was observed in NK cells at E:T cell ratios of 25:1 or more ($p < 0.0001$) and in macrophages at E:T cell ratios of 50:1 or more compared to the corresponding values in the absence of effector cells ($p = 0.001$ at 50:1; $p < 0.0001$ at 100:1) (Fig. 2). CD4+T cells and CD8+T cells did not have cytotoxic effects on NP cells.

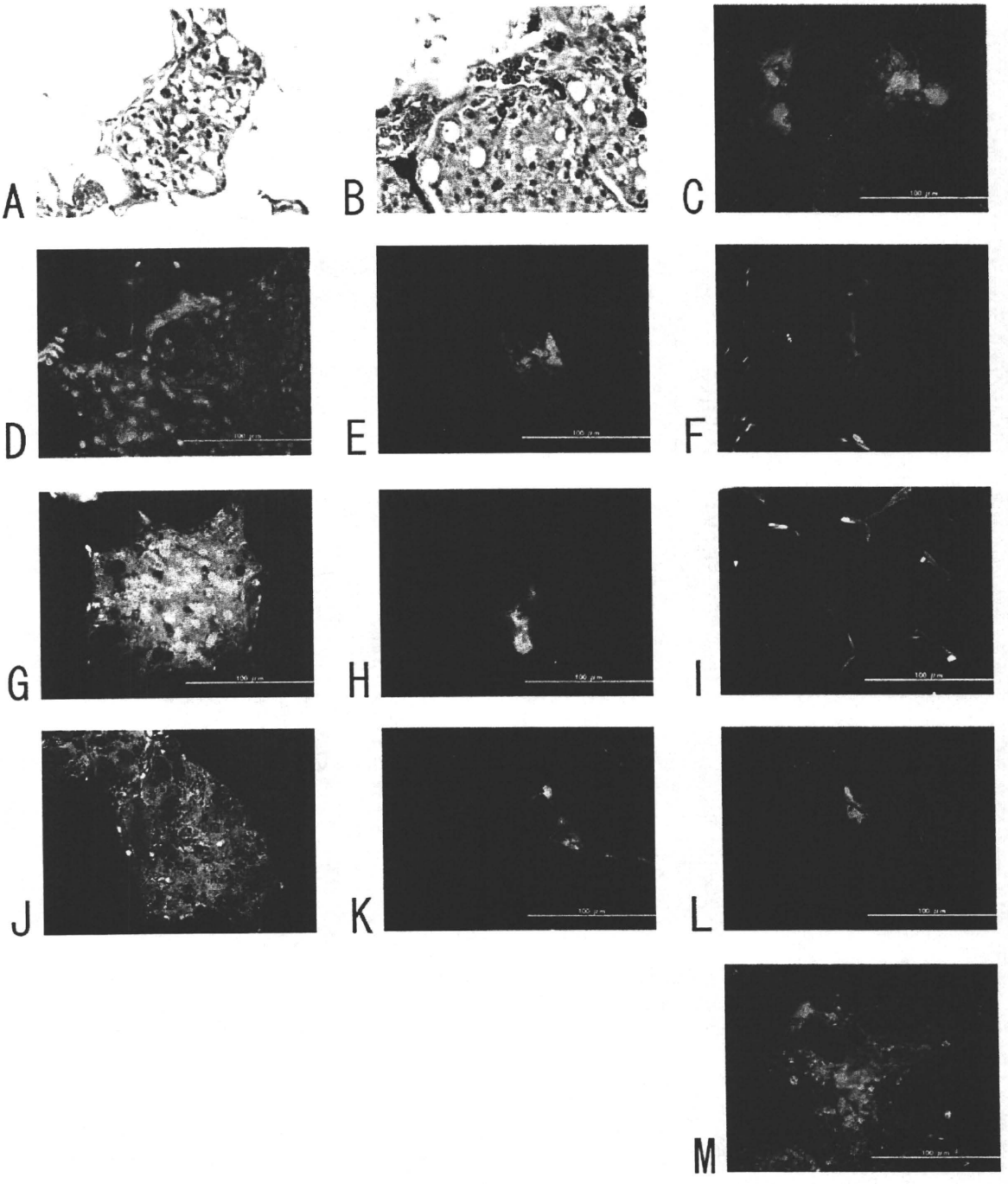

Fig. 4. Histological analysis of NPs at the transplant site of recipient rats. HE (A), safranin-O (B) and keratan sulphate IHC (C) staining indicates the presence of transplanted NPs at day 5. Safranin-O stains the proteoglycan of NPs (Red), and keratan sulphate is specific extracellular matrix of NPs (Green). Keratan sulphate was stained even 26 days after transplantation in the recipient of NOD mouse (M).

CD3 (D~F), CD68 (G~I) and CD161 (J~L) (Red) are immunohistochemically double-stained with keratin sulphate (Green). D, G, and J are the results at day 5; E, H, and K at day 10; F, I, and L at day 40. Keratan sulphate decreased dependent on time, NK cells and macrophages decreased simultaneously.

To summarize, the results of the *in vitro* CFI and cytotoxicity assays revealed the presence of a spleen cell population that had cytotoxic effects on autologous NP cells. This cytotoxic spleen cell population is composed of sub-populations of NK cells and macrophages. Furthermore, as a negative control of cytotoxicity assay, we used fibroblast-like cells of *annulus fibrosus* origin. The result was that the fibroblast-like cells was tolerant to isogeneous spleen cells, however *nucleus pulposus* cells was sensitive. This result raised our test hypothesis that NP is sensitive to specific immune cells.

***In vivo* study**

BLI study. We performed a BLI study to investigate immunological responses to transplanted NP tissues *in vivo*. The BLI evaluation showed a significantly higher survival rate for transplanted NP cells in the Lew-NOD group compared to that in the Lew-Lew group totally ($p = 0.036$), at day 7 (0.35 ± 0.18 *vs.* 0.11 ± 0.05; $p = 0.042$) and at day 21 (0.16 ± 0.08 *vs.* 0.03 ± 0.02; $p = 0.037$) (Fig. 3A). After 90 days, up to 13% of the transplanted NP cells had survived in the Lew-NOD group (Fig.3B). NP cells transplanted into Lewis rats (Lew-Lew) did not survive past 21 days, when luminescence at the NP cell transplant site had decreased to near background levels (Fig.3C).

IHC staining. Because our results showed that transplanted NP cell survival was reduced in association with an immunological reaction, we used immunological staining to identify which types of immune cells had infiltrated. Transplanted NP tissues in rats at day 5 existed mainly in the loose subcutaneous fat tissue as an agglomeration of cells with a bubble-like extracellular matrix (Fig. 4A). Safranin-O staining showed the presence of red-stained proteoglycans (Fig. 4B), and fluorescent green-stained keratan sulphate, both of which are constituents of the extracellular matrix of the NP (Fig. 4C). We observed transplanted NP tissues at day 5 (Fig. 4D, G, J), however, the amount of transplanted NP tissue was markedly decreased at day 10 in the Lewis rats, while NP tissue was obviously present in NOD mice recipients even at day 26 (Fig. 4M). From the IHC evaluation of immune cells in Lewis rats, no CD3 positive T cells attraction were observed subcutaneously from day 5 to day 40 (Fig. 4D, E, F). Attraction of NK cells and macrophages was observed at days 5 and 10 around the outgrown NP tissues (Fig. 4G, H, J, K); however, neither NP tissues nor immune cells were observed at day 40 (Fig. 4I, L). The numbers of NK cells and macrophages in microscope fields that included agglomerated NP cell clusters decreased with time (Table 2).

Discussion

The precise mechanism of immunological involvement in the pathology of disc herniation has not been defined. We performed two immunological assays, the CFI and the cytotoxicity assay, using co-cultured NP and immune cells. We also developed an *in vivo* subcutaneous transplantation model and measured the survival rate of transplanted NP cells using the BLI method. IHC at the transplant site of the recipient rats was used to identify the immune cells.

The suppression of NP cell colony formation was observed to be dependent on the effector:target (E:T) cell ratio. We found that non-adherent (CFU-NA) colonies were more strongly suppressed by immune cells than adherent (CFU-A) colonies. Because NP cells are known to be heterogeneous (Chelberg *et al.*, 1995), this difference in colony formation may reflect the different epitopes recognized by immune cells, or possible differences in the immune privilege function, like the presence or absence of Fas ligand. Based on these possibilities, about 20% of the NP cell population were alive even at E:T cell ratio of 100:1, which appears to differ immunologically from other NP cells. Of particular interest was the assessment of direct

Table 2 The number of immune cells in a microscope field (x40)

	Day 5	Day 10	Day 40
T cell	None	None	None
NK cell	2-5	1	None
Macrophage	4-7	1-3	None

This table indicates the number of representative agglomerated NP cell clusters in the tissue specimen of transplanted site in Lewis rats. NK and macrophage cells were observed in the transplanted site in the early phase, whereas T cells were not observed. In day 40, neither NP tissues nor immune cells were observed.

cytotoxic function of the immunological cell types. The results of the cytotoxicity assays of isolated T, NK, and macrophage cells demonstrated that only the NK and macrophage cells had cytotoxic activity on NP cells. The target molecules and their location on the NP cells remain undefined; further biological and immunological studies are necessary.

The results of the BLI study showed differences in the survival rate of NP cells in the transplanted NP tissues between the Lewis rat and NOD mouse recipients. NP cells are known to undergo apoptosis (Park *et al.*, 2001), and intervertebral disc cells are thought to be able to behave as competent phagocytes (Jones *et al.*, 2008). However, these results do not explain the different survival rates of NP cells in the current study. Because the survival rate of NP cells was higher in immunodeficient mice than in Lewis rats, immunological functions are implicated. NOD/shi-scid mice lack mature lymphocytes, and have macrophage dysfunction, a reduced level of NK cell activity and absence of circulating immune components compared to wild-type mice. These factors may account for the difference in NP cell survival rate between NOD mice and Lewis rats in our study.

We also detected the infiltration of specific immune cells into the NP transplant sites; these results definitively demonstrate the immunological activity of these cell types against NP tissues. Macrophages and NK cells, but not T cells, were detected, although the presence of T and B cells in isolated human herniated discs and in experimental porcine models has been previously reported (Geiss *et al.*, 2007). Our results suggest an early immunological response after normal NP tissues were exposed to the immune system. Thus, macrophages and NK cells were observed on days 5 and 10 when residual NP was present, but not on day 40 when the transplanted NP had disappeared. This finding supports the presence of an immunological response to transplanted NP tissues.

In our IHC study, CD68 positive cells did not resemble the appearance of resident chondrocytes. Although Jones *et al.* (2008) suggested that CD68 positive cells were transformed resident intervertebral disc cells, based on their morphology, the results of our study show that these macrophages are not transformed resident cells but rather are infiltrating cells.

Autologous tissues are generally not recognized as foreign by the immune system. The NP is an immune-privileged tissue isolated from the immune system (Hiyama *et al.*, 2008) and it, like similarly isolated tissues, including the eye and testis, can produce inflammatory autoimmune responses (Wildner and Diedrichs-Möhring, 2004; Schuppe and Meinhardt, 2005). Another possible trigger for autoimmunity is innate immunity, which is induced by chemical factors without specific antigen-antibody responses, leading to rapid immune responses to pathological microbe antigens. Because the NP cell produces chemical factors and the carbohydrate structure of the extracellular matrix produced by NP cells may mimic that of pathological microbe antigens, the NP may trigger an innate immunity response (Bárdos *et al.*, 2005).

In the *in vivo* transplantation model, we utilized a xenogeneic model because the mouse is too small to obtain enough donor NP cells. The use of NOD mice as recipients is well established for evaluating the effects of immunodeficiency. In addition, the xenogeneic transplantation model is commonly used for immunological evaluation (Yoshino *et al.*, 2000).

In conclusion, even non-degenerated NP cells elicit an immune response, and macrophages and NK cells in particular are shown to have an early immunological function when NP cells are exposed to the immune system. While these results may not be directly applicable to the human, this study provides important information for understanding the pathophysiological mechanism of disc herniation.

Acknowledgements

This work was supported in part by a Grant-in-Aid for Scientific Research and a Grant of The Science Frontier Program from the Ministry of Education, Culture, Sports, Science and Technology of Japan (D.S. and J.M.), grants from AO Spine International (D.S.), and Jichi Medical University.

References

Bárdos T, Szabó Z, Czipri M, Vermes C, Tunyogi-Csapó M Urban MR, Mikecz K, Glant TT (2005) A longitudinal study on an autoimmune murine model of ankylosing spondylitis. Ann Rheum Dis **64**: 981-987.

Bobechko WP, Hirsh C (1965) Auto-immune response to *nucleus pulposus* in the rabbit. J Bone Joint Surg Br **47**: 574-580.

Burke JG, Watson RWG, McCormack D, Dowling FE, Walsh MG, Fitzpatrick JM (2002) Spontaneous Production of Monocyte Chemoattractant Protein-1 and Interleukin-8 by the Human Lumbar Intervertebral Disc. Spine **27**: 1402-1407.

Chelberg MK, Banks GM, Geiger DF, Oegema TR Jr (1995) Identification of heterogeneous cell populations in normal human intervertebral disc. J Anat **186**: 43-53.

Doita M, Kanatani T, Ozaki T, Matsui N, Kurosaki M, Yoshiya S (2001) Influence of macrophage infiltration of herniated disc tissue on the production of matrix metalloproteinases leading to disc resorption. Spine **26**: 1522-1527.

Geiss A, Larsson K, Rydevik B, Takahashi I, Olmarker K (2007) Autoimmune Properties of *Nucleus Pulposus*: An Experimental Study in Pigs. Spine **32**: 168-173.

Geiss A, Larson K, Junevik K, Rydevik B, Olmarker K (2008) Autologous *nucleus pulposus* primes T cell to develop into interleukin-4-producing cells: an experimental study on the autoimmune properties of *nucleus pulposus*. J Orthop Res **27**: 97-103.

Gertzbein M, Tail M, Gross A, Falk R (1975) Autoimmunity in degenerative disc disease of the lumbar spine. Orthop Clin North Am **6**: 67-73.

Haro H, Craford HC, Fingleton B (2000) Matrix metalloproteinase-7–dependent release of tumor necrosis

factor-α in a model of herniated disc resorption. J Clin. Invest., **105**: 143-150.

Hiyama A, Mochida J, Iwashina T, Omi H, Watanabe T, Serigano K,Tamura F, Sakai D (2008) Transplantation of mesenchymal stem cells in a canine disc degeneration model. J Orthop Res **26**: 589-600.

Ikeda T, Nakamura T, Kikuchi T, Umeda S, Senda H, Takagi K (1996) Pathomechanism of spontaneous regression of the herniated lumbar disc: Histologic and immunohistochemical study. J Spinal Disord **9**: 136-140.

Jones P, Gardner L, Menaga J, Williams G, Roberts S (2008) Intervertebral disc cells as competent phagocytes *in vitro*: implications for cell death in disc degeneration. Arthritis Res Ther **10**: R86.

Kang JD, Georgescu HI, McIntyle-Larkin L, Stefanovic-Racic M, Donaldson WF 3rd, Evans CH (1996) Herniated lumbar intervertebral discs spontaneously produce matrix metalloproteinases, nitric oxide, interleukin-6, prostaglandin E2. Spine **21**: 271-277.

Katsuno R, Hasegawa T, Iwashina T, Sakai D, Mikawa Y, Mochida J (2008) Age-related effects of cocultured rat *nucleus pulposus* cells and macrophages on nitric oxide production and cytokine imbalance. Spine **33**: 845-849.

Le Maitre CL, Hoyland JA, Freemont AJ (2007) Catabolic cytokine expression in degenerate and herniated human intervertebral discs: IL-1**b** and TNF**a** expression profile. Arthritis Res Ther **9**: R77.

McCarron RF, Wimpee MW, Hudkins PG, Laros GS (1987) The inflammatory effect of *nucleus pulposus*. A possible element in the pathogenesis of low back pain. Spine **12**: 760-764.

Nachemson A (1969) Intradiscal measurements of pH in patients with lumbar rhizopathies. Acta Orthop Scand **40**: 23-42.

Park BJ, Chang H, Kim K (2001) Expression of Fas ligand and apoptosis of disc cells in herniated lumbar disc tissue. Spine **26**: 618-621.

Park JB, Chang H, Kim YS (2002) The pattern of interleukin-12 and T-helper types 1 and 2 cytokine expression in herniated lumbar disc tissue. Spine **27**: 2125-2128.

Satoh K, Konno S, Nishiyama K, Olmarker K, Kikuchi S (1999) Presence and distribution of antigen-antibody complexes in the herniated *nucleus pulposus*. Spine **24**: 1980-1984.

Schuppe HC, Meinhardt A (2005) Immune privilege and inflammation of the testis. Chem Immunol Allergy **88**: 1-14.

Spitzer G, Verma DS, Fisher R, Zander A, Vellekoop L, Litam J (1980) The myeloid progenitor cell – its value in predicting hematopoietic recovery after autologous bone marrow transplantation. Blood **55**: 317-323.

Virri J, Gronblad M, Seitsalo S, Habetemarian A, Kappa E, Karahaju E (2001) Comparison of the prevalence of inflammatory cells in subtypes of disc herniations and associations with straight leg raising. Spine **26**: 2311-2315.

Wang XM, Terasaki PI, Rankin GW Jr., Chia D, Zhong HP, Hardy S (1993) A new microcellular cytotoxicity test based on calcein AM release. Hum Immunol **37**: 264-270.

Weiler C, Nerlich BE, Boos N (2005) Expression and distribution of tumor necrosis factor alpha in human lumbar intervertebral discs: A study in surgical specimen and autopsy controls. Spine **30**: 44-53.

Wildner G, Diedrichs-Möhring M (2004) Autoimmune uveitis and antigenic mimicry of environmental antigens. Autoimmun Rev **3**: 383-387.

Yoshino H, Ueda T, Kawahata M, Kobayashi K, Ebihara Y, Manabe A, Tanaka R, Ito M, Asano S, Nakahata T, Tsuji K (2000) Natural killer cell depletion by anti-asialo GM1 antiserum treatment enhances human hematopoietic stem cell engraftment in NOD/Shi-scid mice. Bone Marrow Transplantation **26**: 1211-1216.

Establishment and Characterization of Transplantable, Luminescence Labeled Rat Renal Cell Carcinoma Cell Lines

Minoru Kobayashi,* Takashi Murakami, Ryosuke Uchibori, Nicole A. L. Chun, Eiji Kobayashi, Tatsuo Morita and Keiya Ozawa

From the Department of Urology (MK, TM) and Divisions of Bioimaging Sciences (TM, NALC, EK) and Genetic Therapeutics (RU, KO), Center for Molecular Medicine, Jichi Medical University, Tochigi, Japan

Purpose: Since renal cell carcinoma is considered an immunogenic tumor, testing therapeutic strategies has been impeded by the lack of relevant tumor models in immunocompetent animals. Recent advances in bioluminescence imaging permit sensitive in vivo detection and quantification of cells emitting light. Thus, we established bioluminescent rat renal cell carcinoma cell lines for immunocompetent rats.

Materials and Methods: The rat renal cell carcinoma cell line ACI-RCC stemming from chemically induced renal cell carcinoma in syngeneic ACI rats was stably transfected with a recombinant retroviral vector encoding luciferase genes derived from fireflies (ACI-RCC-ffLuc) or click beetles (ACI-RCC-cbLuc). Cell line growth patterns were characterized by bioluminescence imaging.

Results: Linear correlations noted observed between cell number and photon counts in each cell type. ACI-RCC-cbLuc emitted light about 500-fold higher than ACI-RCC-ffLuc. When transplanted subcutaneously, only ACI-RCC-ffLuc grew, possibly because of less antigenicity. ACI-RCC-ffLuc photon emission correlated significantly with subcutaneous tumor size. Orthotopic tumor growth and subsequent metastatic spread were monitored with time by increased photon intensity on bioluminescence imaging. Based on ACI-RCC-cbLuc bioluminescent intensity the in vitro screening test allowed the identification of several anticancer agents, including molecules related to human renal cell carcinoma progression.

Conclusions: The new in vivo rat renal cell carcinoma model with luciferase labeled tumor cells allowed us to monitor tumor growth noninvasively and semiquantitatively by bioluminescence imaging. This model system coupled with in vitro screening permits precise evaluation of tumor behavior in intact animals and determination of the therapeutic efficacy of anticancer agents for renal cell carcinoma.

Key Words: kidney; carcinoma, renal cell; luminescent proteins; cell line; models, animals

Abbreviations and Acronyms

BLI = bioluminescence imaging
cbLuc = click beetle derived Luc gene
DMSO = dimethyl sulfoxide
ffLuc = firefly derived Luc gene
IL = interleukin
Luc = luciferase
RCC = renal cell carcinoma

Submitted for publication May 5, 2009.

Study received animal care and use committee approval.

Supported by a grant from the Health and Labor Science Research Grants from the Ministry of Health, Labor and Welfare (Research on Biological Resources), and the Ministry of Education, Culture, Sports, Science and Technology (Project 20591326, 2008), a grant from the Strategic Research Platform for Private Universities with matching fund subsidy from the Ministry of Education, Culture, Sports, Science and Technology, and a Grant-in-Aid for Scientific Research on Priority Area "Cancer" from the Ministry of Education, Culture, Sports, Science and Technology, Tokyo, Japan.

Supplementary material for this article can be obtained at http://www.jichi.ac.jp/uro/index.html.

* Correspondence: Department of Urology, Jichi Medical University, 3311-1 Yakushiji, Shimotsuke, Tochigi 329-0498, Japan (telephone: +81-285-58-7379; FAX: +81-285-44-6595; e-mail: minoruk@jichi.ac.jp).

RENAL cell carcinoma is a potentially lethal kidney disease. RCC treatment still depends on surgical resectability of the primary tumor but the prognosis in patients with metastatic disease remains poor.[1] Antitumor cytokines such as interferon-α and IL-2 have been used widely to treat metastatic diseases but provided only limited therapeutic benefit.[2] Thus, more effective treatments are needed for metastatic disease.

The advent of molecularly targeted therapy, eg bevacizumab, sorafenib,

0022-5347/10/1835-2029/0
THE JOURNAL OF UROLOGY®

Vol. 183, 2029-2035, May 2010
Printed in U.S.A.
DOI:10.1016/j.juro.2009.12.090

sunitinib and temsirolimus, has improved the prognosis in patients with metastatic RCC, provided unprecedented response rates and significantly increased survival.[3] However, complete tumor regression is sporadic and rare, and most patients ultimately have disease progression even during therapy.[3] Further study is needed to identify more effective agents or combinations of targeted agents that can improve the objective response and hopefully lead to complete remission. Some questions have arisen, including whether there are appropriate therapeutic combinations to maximize efficacy with tolerable toxicity or multitargeted agents to inhibit different target molecules involved in cancer progression and whether it is possible to combine potential targeted agents with conventional cytotoxic chemotherapy or cytokine therapy.

To investigate the efficacy of novel agents or appropriate combinations of existing therapies in vitro and in vivo evaluations are required. Immunocompetent animals with normal immune systems are ideal since RCC is a representative immunogenic tumor. Among recent advances in small animal imaging BLI permits sensitive in vivo detection and quantification of cells specifically engineered to express Luc. BLI enables easy longitudinal quantification of the tumor burden in living animals.[4] To date the Luc transfected murine RCC cell line RENCA, which is well characterized and arises spontaneously in Balb/c mice,[5] is the only cellular source of the BLI model for in vivo study of RCC.[6–8] However, using Luc labeled RENCA cells for in vitro determination is not well documented in the medical literature.

We established a new RCC cell line from immunocompetent rats and modified the cell lines for BLI. Two types of Luc expressing rat RCC cells were created. We report that cells engineered for BLI are available for in vitro culture and in vivo animal experiments. This model system also allows in vitro easy drug screening for potential effective compounds or appropriate drug combinations. Thus, we propose that this cell resource may be of great value to develop RCC therapy in humans.

MATERIALS AND METHODS

Animals and Cells

Six to 8-week-old male inbred ACI rats (CLEA Japan, Tokyo, Japan) were used. All experiments were done in accordance with the Jichi Medical University Guide for Laboratory Animals. NIH3T3 cells were maintained in Dulbecco's modified Eagle's medium (Sigma-Aldrich®) with 10% heat inactivated fetal bovine serum under a humidified atmosphere with 5% carbon dioxide at 37C.

Parental rat renal cancer cells (RCC), previously established from an ACI rat exposed to ferric nitrilotriacetate,[9,10] were maintained in vivo in the subcutaneous space of ACI rats every 2 weeks. To allow these cells to be maintained in culture lethally irradiated NIH3T3 cells served as a feeder layer. Cells were cloned twice by limiting dilution in 96-well plates at a density of 0.1 cells per well and a homogeneous cell population was obtained. A total of 16 clones were isolated and clone 4 was used in subsequent experiments. Established cells, referred to as ACI-RCC cells, were grown in 10% fetal bovine serum-Dulbecco's modified Eagle's medium and used between passages 10 and 25.

Luc Transduced Cell Generation and Cell Growth Assay

Stable Luc expressing ACI-RCC cells (clone 4) were developed by transduction with a recombinant retroviral vector encoding neomycin resistance and ffLuc or cbLuc. Plasmids were derived from pMEI-5Neo (Takara Bio, Shiga, Japan) and pGL3 (Promega®) for ffLuc and pELuc (Toyobo, Osaka, Japan) for cbLuc. ACI-RCC cells were infected with the supernatant from the 293 producer cells in the presence of Polybrene® (8 μg/ml). Transduced cells were selected with G418 geneticin (Invitrogen™) (500 μg/ml). Generated colonies were screened using a Luc assay. To determine bioluminescence activity cells were seeded at a serial concentration in triplicate in 96-well plates and measured using the IVIS™ bioimaging system with the Bright-Glo™ Luciferase Assay System as a substrate according to the manufacturer protocol. Transduced ACI-RCC-ffLuc and ACI-RCC-cbLuc cells were propagated separately in medium containing G418 (500 μg/ml). Cells (1×10^5) were incubated for 96 hours. The total viable cell number was determined by the trypan blue exclusion test every 24 hours using a hemocytometer.

Bioluminescence Imaging

In vivo Luc imaging was done with the noninvasive IVIS in vivo imaging system. One minute after intravenous injection of D-luciferin (30 mg/kg) (potassium salt, Biosynth, Postfach, Switzerland) the signal intensity of emitted photons from Luc expressing tissue was measured with a 1-minute integration time. For ex vivo detection tissues were procured after intraperitoneal injection of D-luciferin (60 mg/kg) and immersed in D-luciferin (300 μl/ml in phosphate buffered saline) for measurement by a Luc assay. Living Image® software was used to analyze the data.

Tumor Models

For the subcutaneous tumor model tumor cells (1×10^6) were injected into the abdominal subcutaneous space in rats. Tumor volume was evaluated using the equation, tumor volume = (length in mm) $\times$ (width in mm)^2/2. For the orthotopic kidney tumor model cells (1×10^6) were suspended in phosphate buffered saline (0.1 ml) and inoculated into the left renal subcapsular space.[10] Obvious tumor was established about 1 week later.

In Vitro Sensitive Compound Screening

The SCADS inhibitor kit comprises 3, 96-well plates, including 288 chemicals that target definitive molecules previously established as inhibitors. Each compound was provided at 2 mM in DMSO in each well with 5 μl. To screen compounds sensitive to ACI-RCC cells ACI-RCC-cbLuc cells were seeded at a density of 2×10^3 in 3, 96-well plates before adding each compound to a final volume of 10 μM. Preparations were incubated for 48 hours. Luminescence intensity was deter-

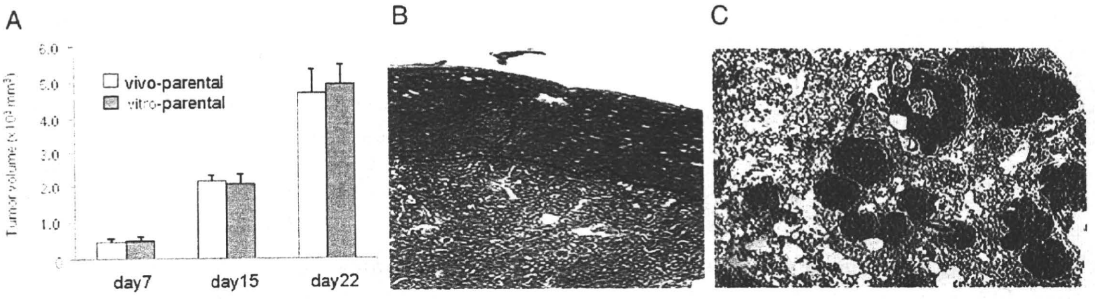

Figure 1. *A*, in vivo growth kinetics of subcutaneous tumor model of original parental cells in vivo and ACI-RCC parental cells in 8 rats each show no difference in in vivo tumor growth rate in 2 cells types. *B*, representative histology of established kidney subcapsular tumor 7 days after tumor cell implantation. Dotted line indicates parenchymal border. H & E, reduced from ×40. *C*, representative histology of lung metastatic foci on day 14. H & E, reduced from ×40.

mined by a luminometer and calculated as a proportion vs the DMSO control alone. An intensity proportion of less than 15% was considered sensitive.

Statistical Analysis

The Student t or Mann-Whitney U test was used to determine p values using StatView® software. Data are expressed as the mean ± SD. Differences between groups were considered significant at $p < 0.05$.

RESULTS

ACI-RCC Line

Characteristics. To permit growth in culture ACI-RCC cells were cultured in the presence of lethally irradiated feeder NIH3T3 cells. A total of 16 clones were isolated and clone 4 was maintained in culture without feeder cells. Thereafter ACI-RCC clone 4 was established as an ACI-RCC line, as described.

To examine whether the established cell line could be transplantable to ACI rats cells (1×10^6) were injected into the subcutaneous space of ACI rats. Visible tumor formed 7 days after tumor inoculation and the tumor growth pattern was equivalent to that of original parent cells, which could only survive in vivo (fig. 1, *A*). Microscopy of the established tumor revealed moderately differentiated carcinoma of the basophilic cell type (fig. 1, *B*). When cells were implanted orthotopically beneath the renal capsule in ACI rats, metastatic spread to the lung also occurred around 2 weeks later (fig. 1, *C*). The animals died 3 to 4 weeks after tumor inoculation.

Establishment. Recent advances in BLI technology have facilitated quantitative analysis of cellular processes in vivo. ACI-RCCs were transduced with ffLuc or cbLuc to visualize tumor progression in vivo. The advantage of using Luc as a marker includes its sensitivity in vitro and its linear dose dependent output of light in the presence of D-luciferin (fig. 2). The photon intensity of ACI-RCC-cbLuc cells was about 500-fold higher than that of ACI-RCC-ffLuc cells at the same cell number. Each cell line had a similar cell proliferation pattern and cell morphology (fig. 3).

ACI-RCC-ffLuc and ACI-RCC-cbLuc BLI

To investigate ACI-RCC-ffLuc and ACI-RCC-cbLuc cell tumor formation cells (1×10^6) were subcutaneously implanted and tumor growth was monitored by BLI and tumor volume measurement. Tumors formed

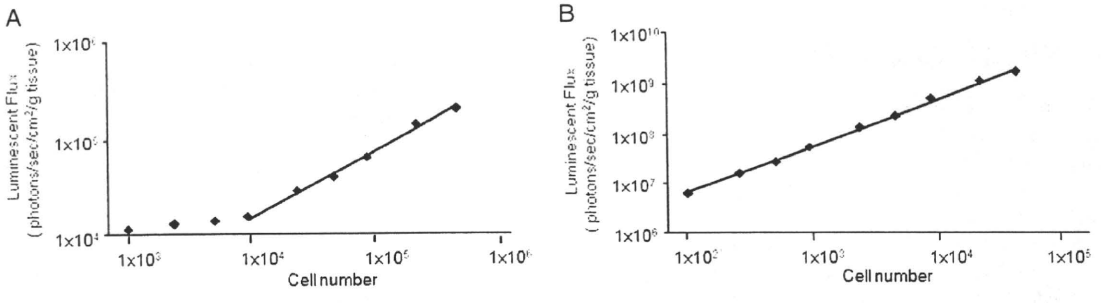

Figure 2. One of 2 independent experiments with similar results shows correlation between cell number and photon intensity using BLI. Cells were seeded at indicated density in triplicate wells and imaged after adding Luc. Mean photon intensity was plotted against cell number per well. Number of cells correlated with amount of emitted light above detection limit. *A*, ACI-RCC-ffLuc cells with 1×10^4 detection limit ($r = 0.997$, $p < 0.001$). *B*, ACI-RCC-cbLuc cells with 1×10^2 cell detection limit ($r = 0.993$, $p < 0.001$). *g*, gm.

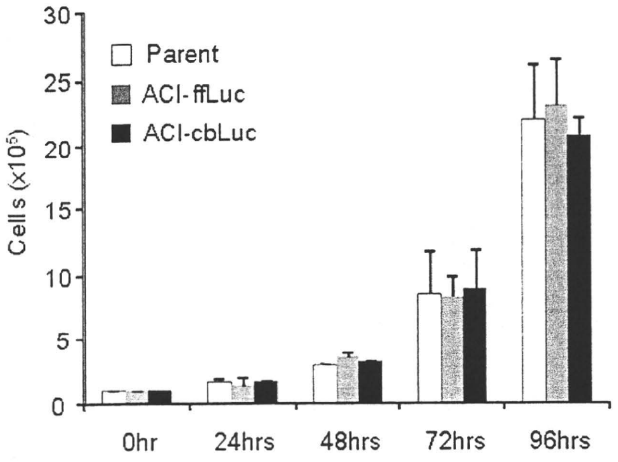

Figure 3. Infection of ACI-RCC cells with pLuc retroviral vectors did not alter cell proliferation rate. Values represent mean of 3 samples in 1 of 2 independent experiments with similar results.

about 1 week after tumor injection of parent ACI-RCC and ACI-RCC-ffLuc cells but no tumors formed after ACI-RCC-cbLuc cell injection. BLI revealed substantial Luc derived photon counts at the implanted site of ACI-RCC-ffLuc and ACI-RCC-cbLuc cells immediately after tumor implantation. Luc activity of ACI-RCC-ffLuc cells generally attained a nadir 24 hours after inoculation and increased to detectable levels by day 7, when tumor was visible (data not shown). However, the strong photon emission from ACI-RCC-cbLuc cells observed for 1 week after injection suddenly vanished at day 9 and tumors of ACI-RCC-cbLuc cells did not form (fig. 4, *A*). The difference in in vivo growth behavior between ACI-RCC-ffLuc and ACI-RCC-cbLuc cells may be due to the antigenicity of cbLuc protein for immunocompetent rats since ACI-RCC-cbLuc cells grew in xenogenic athymic mice (fig. 4, *B*). Results show that ACI-RCC-ffLuc cells are available for analysis of BLI mediated RCC dissemination.

Transduction of the ffLuc gene did not affect the growth kinetics of subcutaneous tumors (fig. 5, *A*). There was significant correlation between tumor size and photon intensity ($r^2 = 0.9825$, $p < 0.001$, fig. 5, *B*). Results indicate the usefulness of this Luc labeled tumor model system as a quantitative tool for growing tumor lesions.

We further evaluated orthotopic tumor growth and metastatic spread using this model. Photon emission was detectable over the tumor site at day 10 and attained a plateau around 3 weeks after orthotopic tumor implantation (fig. 6, *A*). BLI visualized tumor metastasis to the lung about 2 weeks after implantation and photon counts also increased at metastatic sites (fig. 6, *B*). Ex vivo luminescence analysis showed that the tumor burdened kidney and the metastasized lungs in rats were substantially Luc positive (fig. 6, *C*).

Easy In Vitro Screening of Compounds Sensitive to ACI-RCC Cells

While ACI-RCC-cbLuc cells were potentially immunogenic in immunocompetent ACI rats, the strong photo emission potential may allow sensitive drug screening. To address this we investigated whether ACI-RCC-cbLuc cells are available for in vitro drug screening. ACI-RCC-cbLuc cells (2×10^3) were plated on 96-well plates before the compound was added and then incubated for 48 hours. Luminescence intensity was simply determined by a luminometer and calculated as a proportion vs the DMSO control alone. Of the 288 compounds arrayed in the SCADS inhibitor kit 21 showed decreased

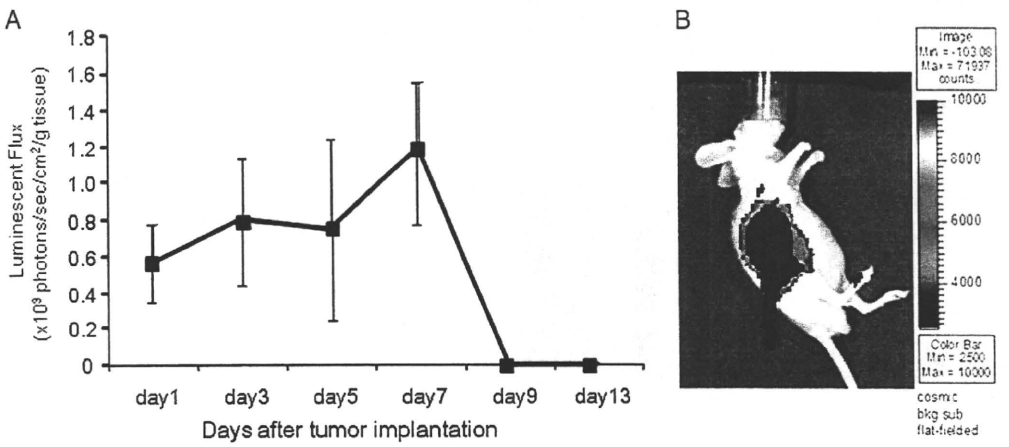

Figure 4. BLI monitoring of subcutaneously implanted ACI-RCC-cbLuc cells. *A*, 1 of 2 independent experiments in 5 rats each with similar results shows abolished strong photon emission 9 days after cell implantation with tumor formation never confirmed. *g*, gm. *B*, representative BLI of ACI-RCC-cbLuc cells 10 days after cell implantation in Balb/c-nu/nu mouse reveals prominent photon emission from established tumor site.

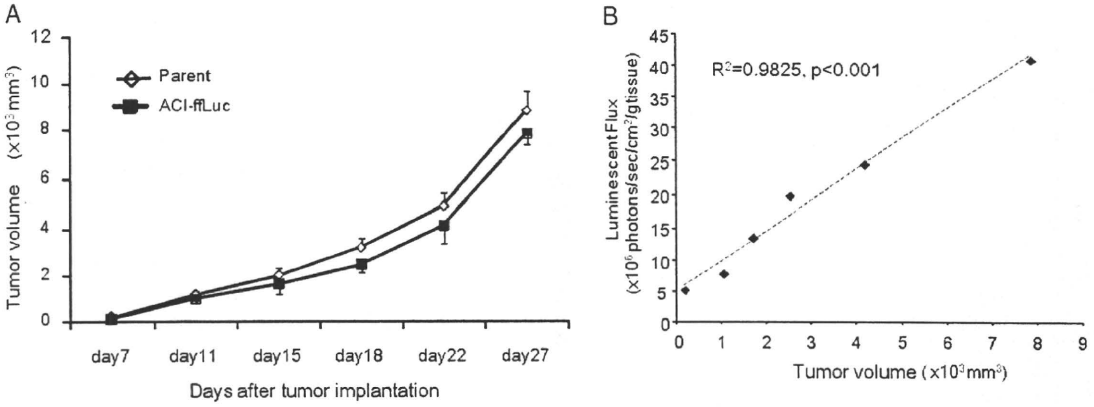

Figure 5. BLI monitoring of subcutaneously implanted ACI-RCC-ffLuc cells. *A*, in vivo growth kinetics of subcutaneous tumor model of parental and ACI-RCC-ffLuc cells revealed no difference between cells in in vivo tumor growth. Each experimental group had 8 rats. *B*, bioluminescence intensity and tumor volume correlated significantly. *g*, gm.

photons with less than 15% considered to have inhibitory effects on ACI-RCC cells with control considered 100% (see table). These data suggest that this RCC cell line is useful as a cell resource for easy drug screening. Notably some candidate compounds targeting molecule heat shock protein 90, AKT, Met and platelet-derived growth factor have been used in the clinical setting in patients with RCC.

DISCUSSION

Increased knowledge of cancer progression and therapeutic resistance has identified many gene products involved in apoptosis, proliferation and other vital cell functions. Novel agents directed at these targets have been developed and show promise in vitro but have not always been consistent in vivo. Because RCC is considered an immunogenic tumor, a reliable and quantifiable orthotopic animal model of RCC in normal immune systems is relevant. To our knowledge murine RCC (RENCA) is the only animal model of RCC in immunocompetent syngeneic Balb/c mice. It represents reliable, reproducible growth characteristics and has a metastatic pattern similar to that of RCC observed clinically in humans.[5,11] However, its further use for biomedical research, which requires blood and tissue sampling or treatment models using surgical manipulation, may be restricted due to limitations imposed by body size.[10] Thus, we established the rat RCC cell line derived from a ferric nitrilotriacetate induced renal tumor and in vivo tumor models in immunocompetent ACI rats, providing another useful model in which to study RCC. We also generated Luc expressing cells, which enabled in vivo monitoring of cancer progression by BLI, the most commonly used modality for noninvasive imaging in small animals. Of Luc genes widely used as light emitting reporters we used 2 types, including that of Phototinus pyralis (firefly) and Phototinus plagiophthalamus (click beetle). Each

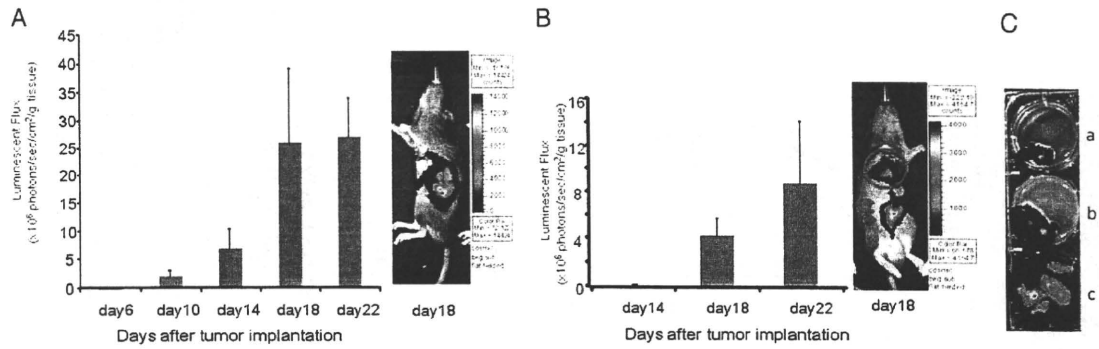

Figure 6. BLI monitoring of orthotopically implanted ACI-RCC-ffLuc cells. *A* and *B*, 1 of 2 independent experiments with similar results. Two of 5 rats in each experimental group died on day 22. *g*, gm. *A*, mean photon intensity of subcapsular tumor with time. BLI shows tumor growing in renal subcapsular space. *B*, mean photon intensity of lung metastatic lesion with time. Representative BLI reveals subcapsular renal tumor (arrows) and lung metastatic lesion (circle). *C*, ex vivo analysis reveals subcutaneous (*a*) and subcapsular (*b*) tumors, and lungs (*c*).